Rock Friction Measurements With Stonegrinder Apparatus

Master's Thesis, 6.12.2016

Author:

Joonas Pylväinen

Supervisors:

Joni Parkkonen
Jussi Timonen

UNIVERSITY OF JYVÄSKYLÄ
DEPARTMENT OF PHYSICS

Tiivistelmä

Pylväinen, Joonas
Kitkamittaukset kivenjauhimella
Pro gradu -tutkielma
Fysiikan laitos, Jyväskylän yliopisto, 2016, 81 sivua

Liikkuvien tektonisten laattojen välillä kitkan oletetaan olevan suuri. Olettamuksen vastaisia havaintoja on kuitenkin tehty useissa tutkimuksissa. Kuuluisin esimerkki on San Andreasin siirros. Siirrosvyöhykkeellä on matala lämmöntuotto, minkä perusteella on arveltu myös kitkan olevan matala. [1] Syynä matalaan kitkaan voivat olla pyöreät kulumapartikkelit, jotka toimivat kuulalaakereiden tavoin [2].

Kitkan tutkimista varten suunniteltiin ja rakennettiin ainutlaatuinen laite, kivenjauhin (engl. Stonegrinder). Kivenjauhimen tarkoitus on jauhaa kahta kairasydäntä toisiaan vasten ja samalla mitata kitkan muutoksia. Laite mittaa jauhamisen aikana vääntömomenttia, josta laskennallisesti saadaan kitkakerroin. Lisäksi kiven lämpötilan muutokset, pyörimisnopeus ja pystysuuntainen siirtymä tallennetaan.

Tutkimusta varten valmistettiin sekä karkea- että sileäpintaisia näytteitä gneissistä. Karkeita näytteitä jauhettiin sekä vakioisen normaalivoiman että vakioisen normaalipaineen alla. Sileät näyteet jauhettiin vakioisen normaalivoiman ja -paineen alla.

Tuloksista havaittiin, että karkeilla näytteillä vääntömomentti ja lämpötilan muutoksen suuruus ovat käänteisesti riippuvaisia paineesta. Kitkakerroin ei osoittautunut olevan riippuvainen paineesta tai lämpötilasta. Röntgentomografialla kuvatut kulumapartikkelit olivat kulmikkaita eikä näytteestä löydetty pyöreitä partikkeleita. Sileäpintaisten näytteiden keskimääräiset vääntömomentit olivat suuria johtuen kulumapartikkeleiden puutteesta jauhamispinnalla.

Avainsanat: Kitka, tribologia, tektoniikka, kivet

Abstract

Pylväinen, Joonas
Rock Friction Measurements With Stonegrinder Apparatus
Master's Thesis
Department of Physics, University of Jyväskylä, 2016, 81 pages.

Friction between large moving tectonic plates is thought to be high but the lack of corresponding frictional heat suggests otherwise [1]. The lack of friction could be explained by smaller rock fragments being rounded and acting as ball-bearings between the plates [2]. To study rock fragmentation and friction a special apparatus called Stonegrinder was built. It grinds two drill core rock samples against each other and measures the changes in friction.

Rough surfaced gneiss samples were ground under two conditions: constant normal force, and constant normal pressure. Smooth surfaced gneiss samples were ground under constant normal force and pressure. Torque and the magnitude of temperature change were found to be inversely dependent on the compressive pressure. The coefficient of friction was independent of pressure and temperature. Wear particles imaged with X-ray tomography were found to be angular instead of spherical. Smooth surfaced samples had high mean torques due to the lack of wear particles.

Keywords: Friction, Tribology, Tectonics, Rocks

Preface

The work conducted in this Master's thesis has been done between January 2015 and November 2016 at the Department of Physics in the University of Jyväskylä.

I would like to thank Jussi Timonen for giving out this interesting topic for my Bachelor's thesis and the opportunity to continue the research in my Master's thesis. In addition, I would like to thank Joni Parkkonen for the frictionless guidance during the project and all the staff of the Department of Physics involved in building the Stonegrinder. Special thanks on the homefront to my lovely Helmi for her continuous support during the entire endeavour.

Jyväskylä 6. December 2016

Joonas Pylväinen

Contents

1 Introduction

Friction is a phenomenon that is a part of everyone's day-to-day life. In engineering friction can be either the solution or the problem. Bearings aim to lower friction and car tyres aim to maximize friction. The study of friction began hundreds of years ago and the basic laws of friction were written in 1699 by Guillaume Amontons (see, e.g. [3]).

Even though friction has been studied for centuries new discoveries are still being made. Latest research suggests that fracturing and friction are not separate phenomena but connected instead. Through "laboratory earthquakes" it was discovered that the friction of two sliding surfaces occurs only after the connections between the surfaces have been broken. At slower rupture velocities classical models for shear cracks were found to be accurate but at higher speeds approaching the Rayleigh wave speed, the rupture speed reached saturation. It remains to be seen how the new discoveries will affect geophysics and friction models. [4] [5]

When massive tectonics plates move the friction is expected to be high, and therefore frictional heat should be high as well. However examples of the opposite behaviour can be found. The phenomenon is called the heat flow paradox. The most famous example of it is the San Andreas fault. The fault has been determined to have low strength and friction which could possible be caused by fault gouge. [1] Spherical wear particles acting as ball-bearings decrease friction but whether they can be formed spontaneously in nature is unknown. [2]

To study the friction of rock surfaces an apparatus called Stonegrinder was designed. The basic function of it is to grind surfaces of two drill core samples against each other while saving data from several different sensors. The most important parameter is the measured torque from which the coefficient of friction is calculated. For simplicity only classical Amontons' laws are used as base for the calculations. Although the measurement setup is highly experimental the aim is to receive data which could explain how wear particles affect friction.

2 Theory

2.1 Geological Background

The purpose of this chapter is to explain some basic concepts of geology and geophysics related to tectonics and friction. The background of this thesis is in plate tectonics and the basics of it are presented in chapter 2.1.1, based for the most part on reference [6]. Deformation of rocks and the lack of frictional heat during tectonic events are explained in chapters 2.1.2 and 2.1.3. Properties of gneiss, based mostly on reference [7], are presented in chapter 2.1.4. In addition the nature of the drill core samples from Olkiluoto is discussed.

2.1.1 Plate Tectonics

Plate tectonics is a relatively new theory since the first parts of this unified theory were published during the 1960s (see, e.g. [6]). Currently it is the accepted theory for explaining the Earth's major surface features.

The Earth is mostly comprised of iron Fe, silicon Si, magnesium Mg and oxygen O. The core of the Earth is iron/nickel and it is surrounded by the mantle and the crust which are mostly comprised of silicates. Pressure increases inside the Earth approximately 30 MPa/km when going deeper. The pressure is caused by overlying material and tectonic forces.

The lithosphere comprising of the crust and the upper mantle is divided into tectonic plates. For example Finland resides on one of the major plates, i.e. the Eurasian plate. There are 15 major tectonic plates (fig. 1) which can be distinguished by their relative motions. Other smaller plates exist but they are not as simple to define due to their fused boundaries.

According to the expanding Earth hypothesis the lithosphere was originally continuous. Expansion of the Earth caused the lithosphere to fragment. Due to the expansion, empty spaces were left between the fragmented parts which were filled with material from the mantle. These filled gaps formed ocean floors.

The driving force of the tectonic plates is thermal energy. Heat is generated in the core and it is transferred towards the surface through convection in the mantle which causes

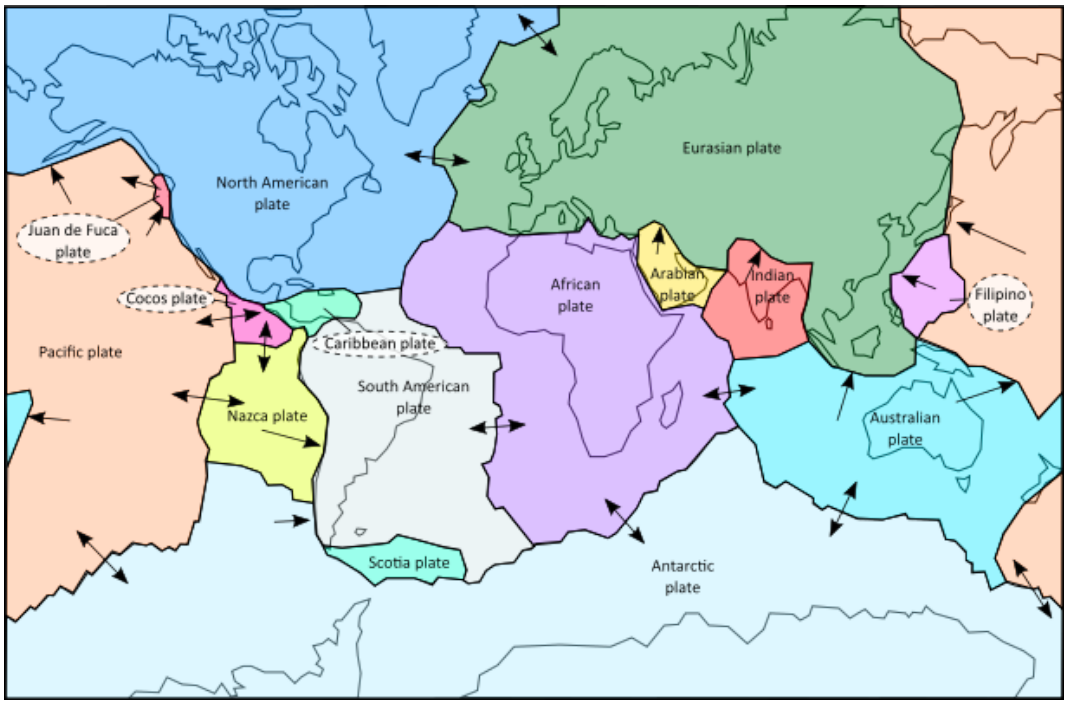

Figure 1. *Major tectonic plates and their relative motions. [6, p. 96]*

matter to flow. This convectional flow moves the tectonic plates in different directions causing them to collide or diverge. Diverging tectonic plates such as the North American plate and the Eurasian plate spread the sea floor on site of the Mid-Atlantic Ridge. Collision of tectonic plates can form mountain ranges such as the Himalayas. Tectonic forces cause stress which results in faulting if the internal strength of the rock is exceeded. Faults are discontinuations of rock material and their size can vary from micrometres to thousands of kilometres. Relative movement along the fault plane occurs when built up stress overcomes the static friction of the contacting rock surfaces. [7, pp. 64-80] The relative movement can be fast or slow. Rapid movement over seconds causes earthquakes which generate seismic waves. Slower and steadier movement over several months or years is called aseismic creep since seismic waves are not produced.

2.1.2 Deformation of Rocks

Rheology is the science that studies the flow of materials under stress σ. In rock rheology the time scale is important. Short-term (seconds to days) stress might shatter a rock but longer-term stress might deform it by flowing, i.e. creeping. Creeping is plastic deformation and it is a problem to be considered when using rock as a building material. For example, vertically attached marble slabs deform quickly under their own weight [8, pp. 57-58].

Rocks break under temperature and pressure forming fractures and faults of different scales. Ductile deformation is caused by the flow of material through various mechanisms such as creeping. Importance of ductile flow increases on longer time scales. Brittle deformation through fractures is caused by networked cracks which expand when the strength of the rock is exceeded by the applied stress. Compressional pressure can close cracks and deep below the surface of the Earth all cracks might be closed, and thus producing a more complex situation. Shear fractures or faults form when the critical shear stress σ_s^* is exceeded. The critical shear stress is described by Mohr-Coulomb fracture criterion

$$|\sigma_s^*| = c + \mu\sigma_n \tag{1}$$

where c is the cohesion resisting fracturing by normal stress, σ_n the normal stress, and μ the coefficient of internal friction of the rock. One type of brittle deformation especially related to this thesis is cataclasis.

Cataclasis occurs after repeated shear fracturing which produces increasingly smaller grains that slide or roll against each other. Breccia is a term used for larger grains while gouge is used for more finely grained material. High pressure prevents cataclasis and due to that it mostly occurs in the upper crust. The two mechanisms of cataclasis are microcracking and frictional sliding. Microcracking begins with nucleation, i.e. accumulating dislocation of crystal planes, and continues with propagation of the crack. [9, pp. 7-10] Sliding friction and the wear related to it is further discussed in chapters 2.2 and 2.3.

2.1.3 The Heat Flow Paradox

Friction and the generation of frictional heat along a fault plane is expected to be high but it is not always the case, thus creating so-called "heat flow paradox". The lack of anomalous heat flow during earthquakes and aseismic creep was first discovered in studies regarding the San Andreas fault [1]. The San Andreas fault is thought to be a weak fault, i.e. the fault strength is low and the stress required to initiate a slip is low [10]. The exact nature of the phenomenon is unknown but, for example, fault gouge is suspected to have an impact [1]. Low friction has also been observed in other faults. In studies regarding the Tohoku-Oki fault a residual temperature anomaly of the March 2011 earthquake was recorded at the plate boundary. Based on the temperature anomaly an apparent coefficient of friction was calculated to be 0.08. [11]

Numerical models made by Mora and Place have shown that when gouge is present both heat generation and average fault friction $\bar{\mu_f}$ are low. The more spherical the gouge is, the lower the friction. [12] Mature fault gouge is more spherical because it has undergone several displacements. In practice the mineral composition also effects the shape of the gouge, for example, quartz and feldspar produce different shaped grains. [13] Hexagonal fault gouge yields the lowest average fault friction ($\bar{\mu_f} \approx 0.5$) while in the case of more angular gouge the friction is slightly higher ($\bar{\mu_f} \approx 0.6$). When no gouge is present average fault friction is high ($\bar{\mu_f} \approx 0.9$). [12]

Intrinsic friction μ^* between the grains also has an effect. With gouge present, intrinsic friction seemed to be more or less independent of the average fault friction. When no gouge was present average fault friction increased synchronously with intrinsic friction. The fault friction decreases because the grains roll during slip due to the higher μ^*. With lower intrinsic friction the grains slide instead of rolling. It is possible for the fault friction to be lower than the intrinsic friction. In that instance the fault is weak. Mora and Place point out that the natural occurrence of rolling grains in faults requires further research. [12]

The formation of rolling grains, or spherical wear particles, is possible during sliding. In engineering applications it has been found that metal particles formed by adhesive wear can be trapped in surface cavities and burnished smooth. Continuous sliding to the same direction might dislodge the particle from the cavity and prevent the burnishing process. [14] Computer models made by Åström and Timonen show that in densely packed granular

system the formation of ball-bearing grains occurs when grains are allowed to fragment. A perfectly space-filling system of bearings was not achieved but the maximum fraction of spontaneously formed ball-bearing grains was 0.4. [2]

A different theory suggests that the frictional heat is masked consequently making it impossible to detect. Variable thermal conductivity of the heterogeneous rock material reduces the total conductivity, thus it effects as an insulator. In simulations made by So and Yuen the surface heat was found to be 30 % to 50 % lower due to the variable thermal conductivity. The insulating effect might enhance rock melting, thus reducing the fault strength. [15]

2.1.4 Classification and Properties of Gneiss

Gneiss is a metamorphic rock recrystallized, for example from igneous granite, under the effects of pressure and temperature. Typically gneisses have banded structure, i.e. parallel veins of different coloured minerals. During metamorphosis the mineral composition of the rock might change but in the case of granite it remains relatively unchanged.

Orthogneisses are formed from igneous rocks, such as granite. Paragneisses are formed from sedimentary rocks. The additional classification of gneisses and other metamorphic rocks depends on the texture and the mineral or chemical composition of the rock. The main minerals present in gneiss are quartz, feldspars and micas.

Quartz and feldspars are tectosilicates and they have a tetrahedral silicate structure. Quartz has a repeating structure of SiO_2 and it is colourless but contaminants cause discolouration. Silicon atoms in the structure can be replaced by aluminium atoms which causes a charge difference that attracts K-, Na-, and Ca-atoms. These new structures are called feldspars. They include potassium feldspar (K-feldspars) and plagioclase feldspars (Na- and Ca-feldspars). Feldspars are commonly found in colours of white, grey and red.

Biotite $K(Mg,Fe)_3(Al,Fe)Si_3O_{10}(OH,F)_2$ is a common mineral of the mica group and it is usually black. Many other minerals, besides quartz, feldspars, and micas, exist and depending on the rock type some maybe more abundant than others. Some common minerals and their colour variations are presented in table 1. In addition to different chemical formulas minerals of the same chemical composition might have different possible crystal structures.

Common types of gneisses are, for example, granite gneiss, mica gneiss, veined gneiss and augen. Veined gneiss and augen are migmatitic gneisses which are mixtures of

Table 1. Minerals present and their colours in granite and gneiss.

Mineral	Colours
Feldspars	grey, red, pink, white
Quartz	white, grey
Biotite (mica)	black, brown
Muscovite (mica)	white, gold, green
Hornblende	black, brown, green

metamorphic rocks and igneous rocks. Lighter granitic part of these rocks is called leucosome and darker gneissic part is called paleosome. On the edges of the paleosome a dark layer called melanosome might be present. Together leucosome and melanosome are referred as neosome which means newly formed.

The drill core samples used in this study were from Olkiluoto. Extensive geological surveys of the area have been made previously, including a full petrological study "Petrology of Olkiluoto" (ref. [16]), therefore allowing a more detailed discussion of the nature of the samples. The main groups of rocks present in Olkiluoto are: gneisses, migmatitic gneisses, tonalite-granodiorite-granite -gneisses (TGG-gneisses), and pegmatitic granites.

The samples used in this study greatly differ in texture and colour. The different drill cores are categorized as A, B, C, or D depending on their appearance. The darker coloured sample A in figure 2 closely resembles the group of migmatitic gneisses because it has clearly visible veins of lighter neosome and darker paleosome material. The structure is also layered, i.e. foliated. Sample B is a strongly migmatized sample with no clear foliation. The darker areas of the rocks are composed of minerals from the mica group and lighter areas are feldspars and quartz. The coarse-grained sample C in figure 2 could be reddish pegmatitic granite because large individual grains are visible but no clear layers or veins can be distinguished. From table 1 it can be seen that red colouration is caused by feldspars. Sample D is a light coloured sample. The colouration is due to high amounts of light feldspar and quartz. The sample could be a type migmatitic gneiss containing a high amount of leucosome material. More accurate naming of the drill core samples would require determining the exact chemical composition of the rock.

Due to metamorphic processes gneiss is somewhat denser than its precursor igneous granite. The common bulk densities are 2.9 to 3.0 $\mathrm{gm/cm^3}$ and 2.6 to 2.7 $\mathrm{gm/cm^3}$, respectively. Porosity of both rocks is similar, ranging from 0.5 to 1.5 %. [8, p. 29]

Hardness describes the resistance of permanent deformation. Several different scales and methods exist for the measurement of hardness. On Mohs hardness scale gneiss and granite have a value ranging from 6 to 7. Mohs hardness can be used as a rough estimate in some cases. A more scientific scale to quantify hardness is, for example, the Vickers hardness. The unit of Vickers hardness is $\mathrm{kgf/mm^2}$ which can be converted into SI units (GPa) as follows:

$$\frac{HV \cdot 9.806\,65\,\mathrm{m/s^2}}{1000} \tag{2}$$

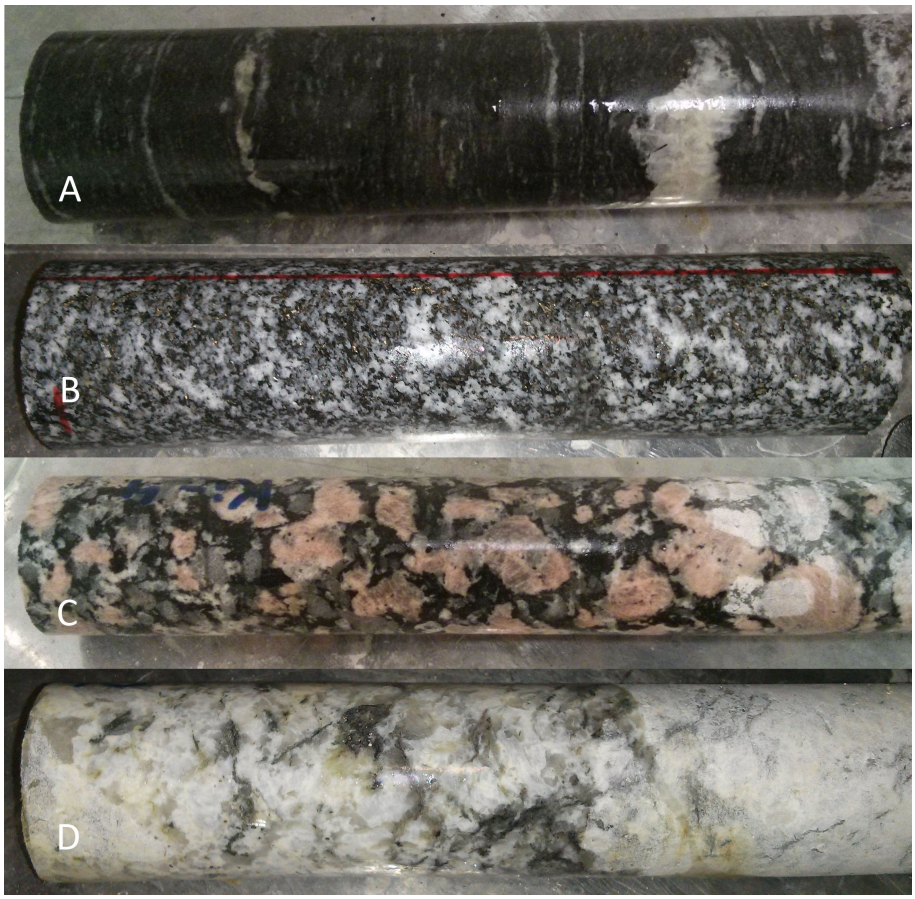

Figure 2. *(A) Drill core sample showing layers typical to migmatitic gneisses. (B) Strongly migmatized drill core sample with no visible layers. (C) Drill core sample showing coarse-grained granitic texture. (D) Drill core sample containing high amounts light coloured feldspar and quartz.*

where HV is the Vickers hardness number [8, pp. 31-33]. Hardness values of gneiss and granite vary between different sources. Some results reported in literature are collected in table 2. Different mineral compositions of the rock samples explain the varying results. The most affecting mineral is quartz because it is hard and it is present in large quantities in gneiss and granite.

Compressive strength is an important parameter in this study since the apparatus presses the rock surfaces together by normal force. Some values reported in literature are presented in table 3. Many properties of rock affect its compressive strength, for example, the direction of foliation and the grain size [8, p. 41]. Considering that the diameter of the drill core is 42 mm the minimum normal force required to shear the drill

Table 2. Hardness of gneiss and granite on different scales.

Rock type	Mohs [8, p. 32]	Vickers [17, p. 56]	Vickers [18, p. 93]	Vickers (avg.) [18, p. 93]
Gneiss	6–7	650–925	382–948	713
Granite	6–7	725–925	720–895	807

core is

$$\begin{aligned} F_{min} = P_{min} \cdot A &= 20 \cdot 10^6\,\mathrm{Pa} \cdot \pi \cdot \left(\frac{0.042\,\mathrm{m}}{2}\right)^2 \\ &= 27\,708.8472\,\mathrm{N} \approx 28\,000\,\mathrm{N}. \end{aligned} \tag{3}$$

The maximum normal force required according to table 3 is

$$\begin{aligned} F_{max} = P_{max} \cdot A &= 150 \cdot 10^6\,\mathrm{Pa} \cdot \pi \cdot \left(\frac{0.042\,\mathrm{m}}{2}\right)^2 \\ &= 207\,816.354\,\mathrm{N} \approx 210\,000\,\mathrm{N}. \end{aligned} \tag{4}$$

The normal force in this instance is exerted by gravity, and therefore the required mass would be approximately 2800 kg–21 000 kg. The engineering limit of the apparatus is 200 kg which is considerably less than the calculated minimum mass. In addition to the normal force, rotational forces are present. The surface aspirations are also expected to be smaller than the total diameter of the drill core. Therefore the used mass can be considerably smaller.

Table 3. Compressive strength of gneiss and granite.

Rock type	Compressive stregth (MPa)[8, p. 40]	Compressive stregth (MPa)[18, p. 50]
Gneiss	20–138	80–140
Granite	20–138	115–150

2.2 Friction

Friction is often described with Amontons' laws because they are sufficient in most cases. In reality more complex models are needed to account for different sources of friction. Neglecting possible sources of friction during experimentation might lead to unexpected material failure or temperature build-up. Therefore, it is important to know what is behind and beyond the basic laws of friction. The information is based for the most part in references [3], [19], and [20].

2.2.1 The Laws of Friction

Friction is a tangential force which resists movement. For example, a building block on an angled surface would not slide down if there was enough frictional force to counter the force caused by gravity. In this instance the friction is called static friction and it keeps the object from moving. Static friction is a response of the system when an external force attempting to move the object is applied. Static friction matches with the force applied up to a certain point, after which the object starts moving as shown in figure 3. The maximum static friction is determined by

$$f_s = \mu_s \cdot f_n \tag{5}$$

where f_s is the maximum static friction, μ_s the coefficient of static friction and f_n the normal force. The coefficient of static friction is dimensionless and determined by the surface material. Static friction can also be expressed by the angle of the inclined plane. When the angle is increased to θ the building block starts to move. The coefficient of static friction expressed by angle is

$$\mu_s = \frac{f_s}{f_n \cos\theta} = \tan\theta \tag{6}$$

where f_n is the normal force, and θ is the angle of the plane, i.e. frictional angle. For coarse grained granite and gneiss the frictional angles are 31° – 35° and 23° – 29°, respectively [21, p. 52] In classical models the coefficient of static friction is constant and material dependent. However recent studies show that static friction is dependent on the applied load [22].

The movement of the object is resisted by kinetic friction which is lower than the maximum static friction ($f_k < f_s$). Kinetic friction force is opposite to the direction of the movement.

The magnitude of the kinetic friction can be described as

$$f_k = \mu_k \cdot f_n \tag{7}$$

where f_k is the kinetic friction and μ_k the coefficient of kinetic friction. In the case of kinetic friction the coefficient is also dependent on the material of the surface. Rolling friction is similar to kinetic friction but the coefficients of rolling friction μ_r are lower.

Static, kinetic and rolling friction are directly proportional to the normal force which is the first law of friction (Amontons' 1st Law). The second Amontons' law states that friction is not dependent on the area of contact (Amontons' 2nd Law). The third law states that friction is also independent of the velocity of the object after it starts moving (Coulomb's Law). These laws are the basis of the Coulomb model of friction which is the most simplest model of dry friction. [23, p. 156]

The three laws are not accurate in all cases. The coefficient of friction itself might be depended on the load and velocity. For example, oxide layers on metals might cause the friction to behave non-linearly under different loads, or high velocities might shear or even melt the surface.

Friction can also be divided into dry friction and fluid friction. Fluid friction is an important aspect of fluid mechanics and lubrication. Dry or "Coulomb" friction is a type of friction which describes the interaction of dry, unlubricated surfaces. It is also the more relevant type of friction considering the topic of this thesis.

2.2.2 Sliding Friction

The Coulomb model of friction presented in the previous chapter 2.2.1 is the simplest model and it applies under dry conditions. In most cases the model is sufficient but it does not take into account complex surface interactions such as deformation and adhesion. For high precision mechanical devices a more realistic model of friction is required. Major factors controlling the friction on dry surfaces are the real area of contact, shear strength of the contacting asperities and the method of shearing [24, p. 14]. The different components contribute to the total amount of friction experienced.

Friction due to adhesion is caused by the bonds formed between contacting asperities. In order to initiate relative motion of the surfaces the bonds have to be broken down first. The bond type and strength depends on the material. Besides the weaker van der

Waals forces, covalent, metallic, or ionic bonds may form between the asperities. For dry contacts the coefficient of adhesional friction is

$$\mu_a = \frac{A_r \tau_a}{W} \tag{8}$$

where A_r is the real area of contact, τ_a the average shear strength of dry contact, and W the normal load. Shear strength of gneiss is $30\,\mathrm{kg/cm^2}$ – $70\,\mathrm{kg/cm^2}$, i.e. $3\,\mathrm{MPa}$ – $7\,\mathrm{MPa}$ [21, pp. 45, 54]. For a filled discontinuity the shear strength is lower and it depends on the type of the filling. More of adhesion and its relation to wear is discussed in chapter 2.3.1.

Difference in hardness of the surfaces in contact causes abrasive wear during sliding. Hard asperities plough the softer surface forming grooves. Ploughing resists the movement of the surface, and therefore causing friction. Amount of friction caused by ploughing is

$$\mu_p = \frac{2 \tan \theta}{\pi} \tag{9}$$

where θ is the angle of attack or roughness angle. The equation does not take into account the accumulation of material in front of the asperity and the angle of attack might be negligible on some surfaces, such as engineering quality metal surfaces [24, p. 16]. On rough surfaces such as sandpaper the component is more significant [14, p. 70].

Deformation of the surface occurs with viscoelastic materials, for example polymers. The surface is deformed by an asperity but as the asperity slides forward the surface behind it recovers. Since materials are not ideally elastic energy losses occur between the initial deformation and recovery. For metals the energy loss due to elastic hysteresis is commonly under 1 %. Considering the drill core samples are solid rock the deformation component in their case can be disregarded.

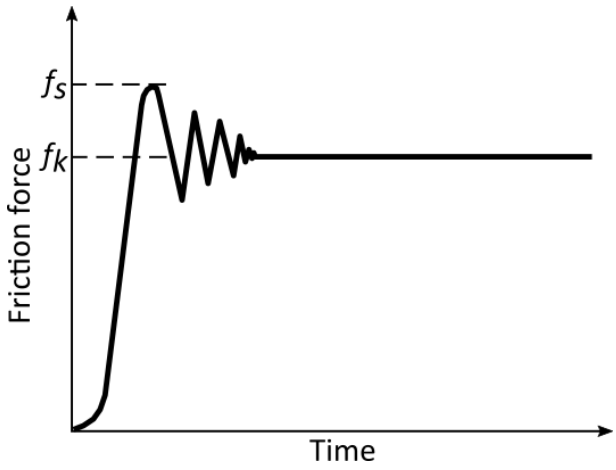

Figure 3. *Friction force as a function of time. Once the static friction force f_s is reached the object's movement initiates, after which the kinetic friction force f_k is required to keep the object moving.*

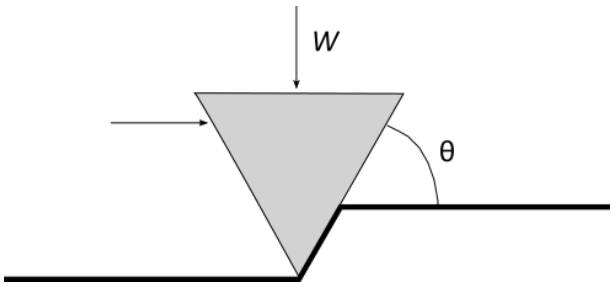

Figure 4. *Simplified presentation of ploughing. Grey asperity digs into the softer surface forming a groove.*

2.3 Wear

Closely related to the topic of friction is wear. Wear is observed when two solid surfaces are in contact and move against each other. Asperities of the surfaces interact during the movement which causes damage to the surface, i.e. displacement or loss of material. High friction does not necessarily lead to high wear. Most of the information presented in the following chapters is based on references [3] and [20].

There are six principal types of wear: adhesive, abrasive, fatigue, impact by erosion and percussion, chemical, and electrical arc-induced. The common factor is the removal of material from the surface.

2.3.1 Adhesive

Adhesion occurs between two contacting surfaces. In solid-solid contact the asperities of the surfaces can form either physical or chemical bonds with each other. Physical bonds are hydrogen bonds or van der Waals forces. Chemical bonds include covalent, ionic, and metallic bonds. Adhesion should not be confused with cohesion. Cohesion is the force holding atoms and molecules together in bulk materials. The bonding mechanisms are the same as with adhesion but cohesion is a property of a continous material, whereas adhesion occurs between two distinct surfaces brought into contact by a normal force. Adhesion contributes to static friction but high adhesion is not a prerequisite for high static friction. Previous studies have shown that static friction can be high even if adhesion is low [25].

Sliding contact causes the bonded asperities to shear. The sheared fragments can attach to the same location or a different location on the surface or agglomerate and form groups of loose wear particles. The mechanism of shearing varies. Adhesion strength is usually lower than the cohesion of the material. Due to that all contacting asperities might not shear (figure 5). The shear can occur on either surface (1 or 2) and the fragment F can attach to the other surface, transfer elsewhere or agglomerate with other fragments. The shape of the fragments formed by this mechanism is irregular or blocky.

In a different mechanism, shearing occurs on a slip line. Plastic shearing forms layers as shown in figure 6. Shear crack advances deeper into surface 1 as more layers are formed. This mechanism produces wedge-shaped fragments.

The amount of adhesive wear can be approximated based on experimental data. The

volume of wear v is dependent on the applied load W, sliding distance x, and surface hardness H as follows:

$$v = \frac{kWx}{H} \tag{10}$$

where k is a dimensionless and material dependent coefficient of wear. Equation 10 is also commonly known as Archard's equation of adhesive wear. Experimental results show that the coefficient of wear is constant within a certain range but, for example with machinery, by exceeding the design limits the coefficient increases with the applied load [26, p. 6]. The equation suggests that wear is not dependent on the contact area but it is proportional to the load. Sliding distance is also a contributing factor but the sliding velocity does not affect the amount of wear according to equation 10. These assumptions correspond with Amontons' laws for the coefficient of friction explained in chapter 2.2.1.

The equation for the average diameter of a loose wear particle formed by adhesive wear is

$$d = 60000 \cdot \frac{W_{ad}}{H} \tag{11}$$

where W_{ad} is the work of adhesion and H hardness [27]. Work of adhesion is the energy per area ($\mathrm{mJ/m^2}$) required to separate two surfaces. The work can be described as

$$W_{ad} = \Delta\gamma = \gamma_1 + \gamma_2 - \gamma_{12} \tag{12}$$

where γ is the surface free energy of surface 1 or 2 and γ_{12} the surface energy of the interface. Experimental results show the surface free energy of silica and quartz to be $193\,\mathrm{mJ/m^2}$ and $220\,\mathrm{mJ/m^2}$, respectively [28]. Since granite and gneiss are mostly comprised of quartz and other silicas their surface free energy could be expected to be the same order of magnitude.

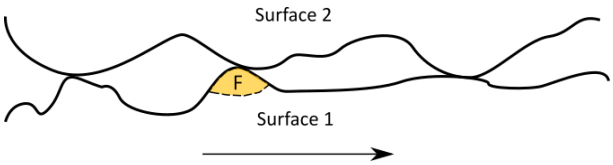

Figure 5. *Adhesive wear mechanism. Surface 1 slides to the direction of the arrow. Adhesive strength is low compared to cohesion and only one asperity shears forming fragment F.*

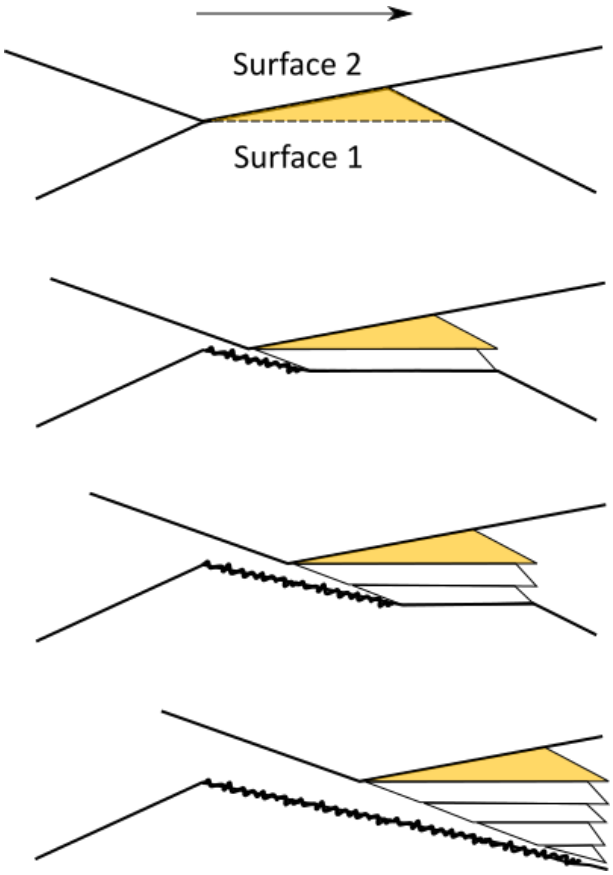

Figure 6. *Adhesive wear mechanism. Surface 2 slides to the direction of the arrow. The first layer (yellow) detaches from surface 1 and attaches to surface 2 along the slip line. More successive layers are detached from surface 1 and attached to surface 2 on top of previous layers. Finally a wedge-shaped fragment is formed.*

2.3.2 Abrasive

Abrasive wear occurs during sliding between a harder surface and a softer surface. Asperities of the harder surface dig into the softer surface and plough a groove parallel to the direction of sliding. The material removed from the groove usually forms loose wear particles. Hard wear particles introduced between softer surfaces can also cause abrasive wear called three-body abrasive wear process. In the situation of the two surfaces the process is called two-body abrasive wear. [27, p. 167]

Common types of abrasive wear are ploughing, wedge formation and cutting (fig. 7). During ploughing material is not removed from the surface but instead displaced to the sides of the groove forming a ridge. Displacement of the material to the sides also occurs during wedge formation but most of the material forms a wedge in front of the tip scratching the surface. Cutting functions similarly but instead of a wedge a ribbon-shaped chip is formed. The parameters affecting most to the amount of wear are the angle of attack and the interfacial shear strength.

To quantify the amount of wear a simplified system is needed. Restricting observations to a single cone-shaped asperity results in simplified situation from where the volume of displaced material can be solved (fig. 8). The volume of displaced material is

$$v = \frac{2Wx\overline{\tan\theta}}{\pi H}, \tag{13}$$

where W is the load carried by the cone-shaped asperity, x displacement of the asperity, $\overline{\tan\theta}$ weighted average of all conical asperities, i.e. roughness factor and H hardness of the softer surface.

2.3.3 Other Types of Wear

Other types of wear include fatigue, impact by erosion and percussion, chemical and electrical-arc-induced wear. Fatigue occurs after repeating cycles of loading and unloading. Surface and subsurface cracks which cause fragmentation form as a result from the loading cycles.

Impact wear can be either erosive or percussive. Erosive wear is caused by streams of solid particles or liquid. Solid particles contacting a surface cause abrasive wear. Liquid droplets hitting a surface at high speeds cause high pressure. Combination of erosion by liquid droplets and corrosion is a problem with mechanical devices such as helicopter rotors. Percussive wear is caused by solid body impacts such as a print hammer striking a piece of paper. It is a hybrid wear mechanism and different wear mechanisms caused by the impact can be observed.

Environmental factors cause corrosion of surfaces. For example, iron is oxidised by the oxygen in air. A chemical film is formed to the surface of the material. Sliding wears the film away and a clean surface is exposed to further corrosion.

Electrical-arc-induced wear is caused by the presence of a high potential over a thin air film during sliding. It causes dielectric breakdown which leads to arcing. Arcing lasts only for tens of microseconds but the power density is on the order of $1\,\mathrm{kW/mm^2}$. Heating occurs on the surface due to the Joule effect and causes melting. Arcing also forms craters and sheared lips to the surface.

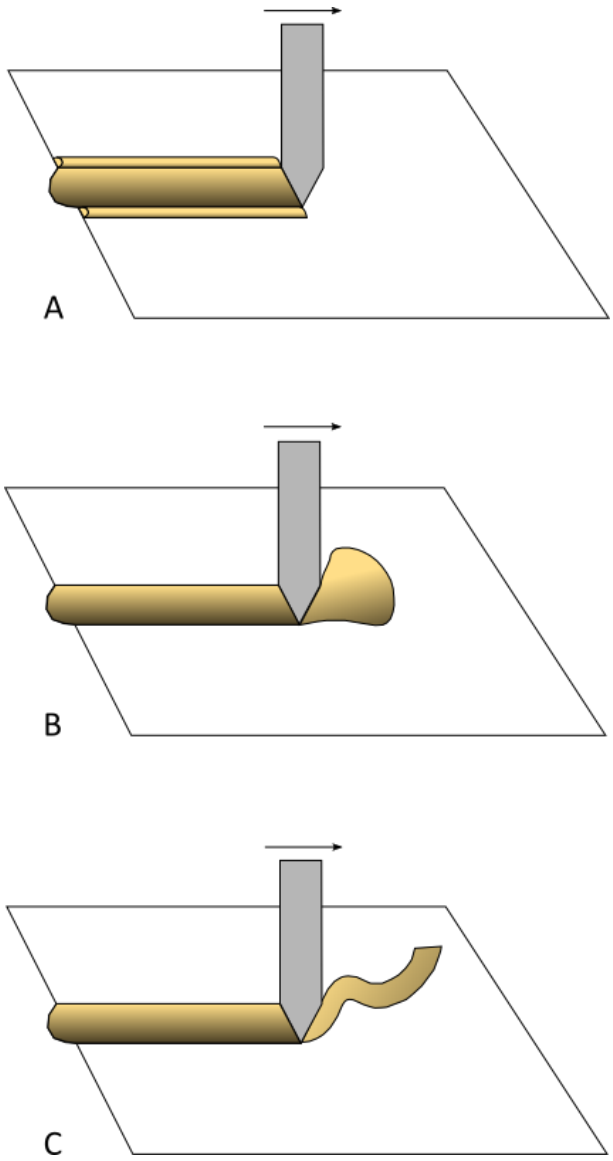

Figure 7. *Common types of abrasive wear. (A) Ploughing tip forming ridges to the sides of the groove. (B) Wedge forming. (C) Cutting tip forming a ribbon-shaped chip.*

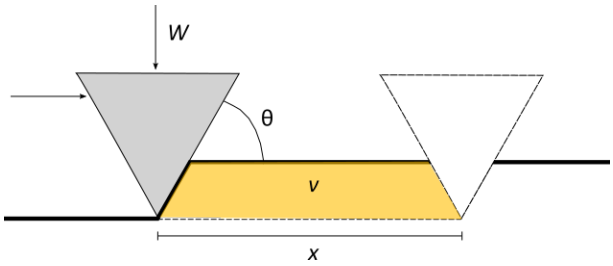

Figure 8. *Abrasive wear caused by a sliding conical asperity. The yellow area is the volume displaced.*

3 Measurement System and Samples

In this chapter detailed information is given about the apparatus and sample preparation. First the mechanical function of Stonegrinder is explained. Derivation of the coefficient of friction is in chapter 3.1.2 and the measurement program is presented in chapter 3.1.3. Chapter 3.2 describes the process used to create the samples.

3.1 Stonegrinder

For the purpose of measuring the friction between two pieces of drill core samples a unique device called Stonegrinder (Fin. *Kivenjauhin*) was built (fig. 9). The following chapters explain the mechanical function and the software of the apparatus in detail.

3.1.1 Apparatus

Stonegrinder is specifically designed to rotate two drill core samples and grind them against each other. A schematic presentation of the apparatus is shown in figure 10. The base structure is assembled from aluminium beams and a large iron disc (blue in fig. 10) acts as a platform for the weights. The platform is mounted on three vertical rails (white beams in fig. 10) from its sides to accommodate the vertical displacement necessary for replacing samples and the displacement occurring during measurements.

Both upper and lower sample holders are mounted in bearings. The lower sample holder is rotated by an electric motor. The upper sample holder would normally rotate with the lower holder but the rotation is prevented by a force sensor (Imada DS2-110) connected to a lever. Since the length of the lever is known it is possible to calculate the torque from the measured force.

Temperature is measured by IRCON's minIRT thermometer directed at the interface of the samples. A microphone is attached on top of the IR thermometer for audio recording. Vertical displacement is measured by a potentiometer located at the side of the rail. Figure 11 shows the sensor setup and the location of the lever.

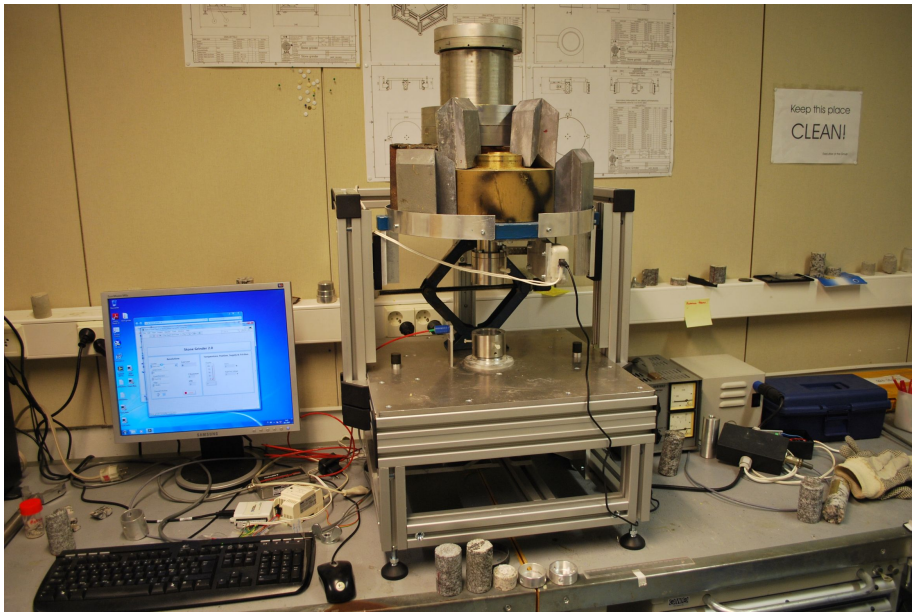

Figure 9. *Stonegrinder measurement apparatus.*

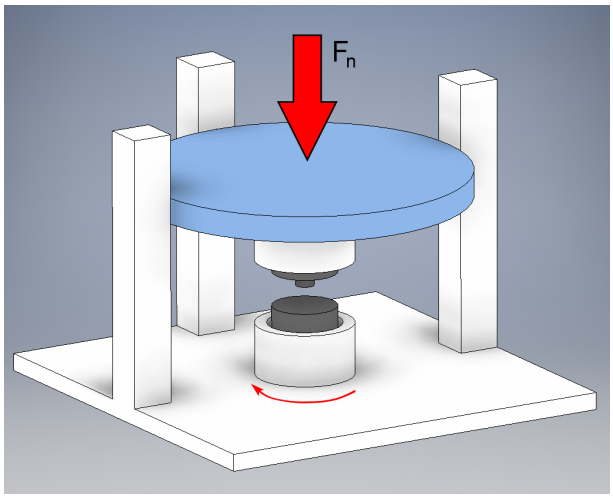

Figure 10. *Schematic presentation of Stonegrinder. The blue disc is the weight platform which carries the load F_n. The two drill core samples are dark grey.*

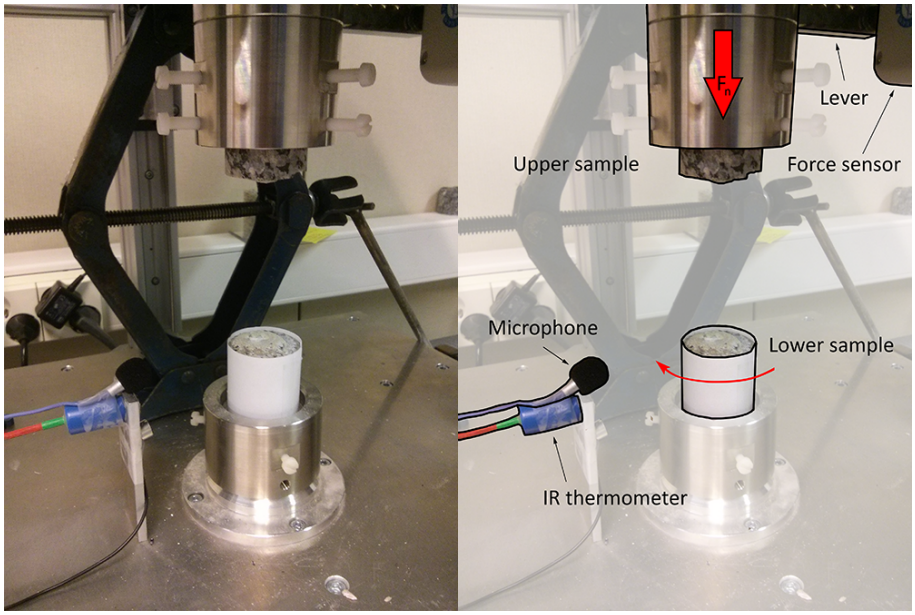

Figure 11. *Close-up photo of the grinding area showing the sensor setup.*

3.1.2 Approximation of the Coefficient of Friction

The coefficient of friction cannot be measured by a probe directly so it has to be derived from other measurable quantities. The most straightforward method is to derive it from the force measured from the rotation axis. To simplify the situation the area of contact is presumed to be constant. In reality the effective area of contact changes constantly and at random, thus making the prediction of change difficult. The direct measurement of the area in real-time is also difficult to achieve and it would require significant changes to the measurement system.

The vertical displacement of the sample due to surface asperities is also another important factor to process. The work required to lift the device's maximum loaded mass M_{max} of 200 kg up 1 mm is

$$\begin{aligned} W_{lift} = M_{max} \cdot g \cdot h &= 200\,\mathrm{kg} \cdot 9.806\,65\,\mathrm{m/s^2} \cdot 0.001\,\mathrm{m} \\ &= 1.961\,33\,\mathrm{J} \approx 2\,\mathrm{J}. \end{aligned} \tag{14}$$

In preliminary test measurements with 200 kg of loaded mass a common value of force F measured from the rotation axis was approximately 100 N. The lever in which the force sensing probe is attached to is 85 mm long ($r_p = 0.085\,\mathrm{m}$). The work required to rotate the 200 kg loaded mass for a full revolution or 360 ° is

$$\begin{aligned} W_{rotation} = \tau \cdot \theta &= F \cdot r_p \cdot \theta \\ &= 100\,\mathrm{N} \cdot 0.085\,\mathrm{m} \cdot 2\pi \\ &= 53\,\mathrm{J} \end{aligned} \tag{15}$$

which is approximately 27 times more than the work required to lift the mass. In addition the vertical back and forth movement cancels itself out in terms of potential energy because an equally large descent follows every ascent [20, p. 329]. The vertical displacement can be thought to be negligible since the movement is in the scale of a few millimetres per revolution and it is not a permanent change of position. [19, pp. 305,351]

The lower drill core sample can be described as an infinite plane and the upper sample as a rotating disc of mass M. Let us take a ring of infinitesimal width dr with a mass of dm from the disc as shown in figure 12. It can be written that the ratio of the ring's mass m to the mass of the disc M is equal to the ratio of the ring's area to the area of the disc as

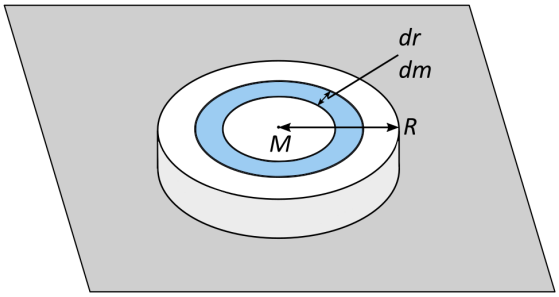

Figure 12. *Simplified presentation of the measurement system. M is the mass of the disc, R the radius of the disc, dm the mass of the infinitesimal ring, and dr the width of the ring.*

follows:

$$\begin{aligned} & \frac{dm}{M} = \frac{\pi(r+dr)^2 - \pi r^2}{\pi R^2} \\ \Leftrightarrow \quad & \frac{dm}{M} = \frac{r^2 + 2rdr + dr^2 - r^2}{R^2}, \end{aligned} \tag{16}$$

where r is the radial distance of the ring's inner edge from the center and R the radius of the disc.

The equal ratios of masses and areas include an approximation that the density of the material is uniform thorough the disc. Since the width of the ring is infinitesimal the term $dr^2 \approx 0$, thus reducing equation 16 into

$$\begin{aligned} & \frac{dm}{M} = \frac{2r\ dr}{R^2} \\ \Leftrightarrow \quad & dm = \frac{2M}{R^2} r\ dr. \end{aligned} \tag{17}$$

The common formula of torque is

$$\tau = r_p \cdot F \cdot \sin\phi, \tag{18}$$

where r_p is the distance from the pivot, F the magnitude of the exerted force, and ϕ the angle of the force [19, p. 351]. Since the angle ϕ is $90\,^\circ$ in this instance the term $\sin\phi$ reduces into 1. The force F is the magnitude of the kinetic friction f_k. Equation 7 states that f_k depends on the kinetic coefficient of friction μ_k and normal force f_n. The normal force exerted on the sample in the measurement setup is gravity. Equation 18 becomes

$$\tau = r_p F = r_p f_k = r_p \mu_k f_n = r_p \mu_k m_u g, \tag{19}$$

where m_u is an unspecified mass. If the final solution of equation 19 is applied to the case of the infinitesimal ring with a mass dm and width dr the equation takes the form of

$$d\tau = r\mu_k g \; dm. \tag{20}$$

Solving dm from equation 20 gives

$$dm = \frac{d\tau}{r\mu_k g} \tag{21}$$

which can be inserted into equation 17. The equation then becomes

$$\begin{aligned} \frac{d\tau}{r\mu_k g} &= \frac{2M}{R^2} r \; dr \\ d\tau &= \frac{2M\mu_k g}{R^2} r^2 \; dr. \end{aligned} \tag{22}$$

Integrating both sides of equation 22 gives

$$\begin{aligned} \int_0^\tau d\tau &= \frac{2M\mu_k g}{R^2} \int_0^R r^2 \; dr \\ \Leftrightarrow \qquad \tau &= \frac{2M\mu_k g}{R^2} \left(\frac{1}{3} R^3\right) \\ \Leftrightarrow \qquad \tau &= \frac{2}{3} M\mu_k g R. \end{aligned} \tag{23}$$

Solving the kinetic coefficient of friction from equation 23 gives the final solution

$$\begin{aligned} \mu_k &= \frac{3\tau}{2MgR} \\ &= \frac{3\tau}{Mgd}, \end{aligned} \tag{24}$$

where τ is the measured torque, M the mass of the disc, and d the diameter of the disc. In practice the torque is calculated from the force measured from the axis of rotation using equation 18. The distance of the sensor from the axis is $r_p = 0.085\,\mathrm{m}$. The mass M is the total mass loaded on top of the upper drill core sample. The diameter d is the diameter of the drill core sample's peak.

3.1.3 Software

The software was made with LabView which is a graphical programming language. The PC interface used to connect all the sensors was NI USB-6008. Through various iterations the program has reached its current state. The basic function of the program is to receive sensor data, transform it and then save it. Front panel of the measurement program is shown in figure 13. During a measurement the front panel shows real-time data of total number of revolutions, revolutions per minute, temperature, measured force, and potentiometer voltage.

The full schematic of the program is shown in figure 14. The two upper while loops acquire and save analog signals, i.e. temperature, force and vertical displacement. The two while loops in the middle acquire digital pulses from the optical encoder and translate it to various quantities, such as RPM. The two lower while loops acquire and save audio from the microphone. To facilitate the large amount of data gathered queues and different save locations are used. The usage of queues allows all of the data to be saved in chronological order without loss due to high sampling rate.

Analog signal acquisition settings are presented in figure 16. Signals are acquired from three different ports. The IR thermometer and the potentiometer signals are in the range of $-10\,\mathrm{V}$ to $10\,\mathrm{V}$ which limits the resolution. Analog input resolution is 12 bits which translates into 4096 steps of $4.9\,\mathrm{mV}$ in the range of $-10\,\mathrm{V}$ to $10\,\mathrm{V}$. In an earlier version of the program all analog inputs were set in the same $-10\,\mathrm{V}$–$10\,\mathrm{V}$ -range causing measured force to have discrete steps in it. The output voltage of the force sensor was converted

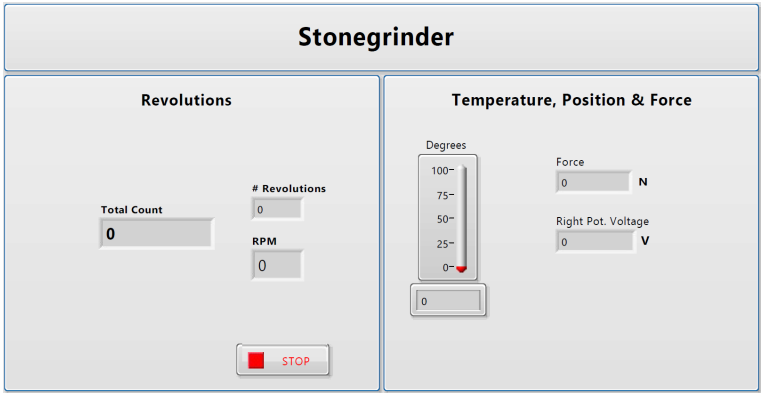

Figure 13. *Front panel of the measurement program.*

into Newtons by multiplying it by 500. Therefore the step size in Newtons was

$$500 \cdot 0.0049\,\mathrm{V} = 2.45\,\mathrm{N}.$$

Changing the voltage range into $-1\,\mathrm{V}$ to $1\,\mathrm{V}$ for the force sensor signal reduced the step size into

$$500 \cdot 0.000\,49\,\mathrm{V} = 0.245\,\mathrm{N}. \tag{25}$$

Sample clock is set to acquire continuous sampling at 100 Hz. The maximum supported sampling rate of the force sensor is 1 kHz but further experimentation showed such a rate to be tasking to the program.

Analog voltage signals are converted into physical quantities differently. Signal from the force sensor is multiplied by 500 to acquire Newtons. Potentiometer voltage signal is saved directly as volts and converted into vertical position later by equation

$$x = V \cdot \frac{206.8\,\mathrm{mm}}{24\,\mathrm{V}}, \tag{26}$$

where V is the measured voltage, 206.8 mm the length of the potentiometer and 24 V the input voltage.

Signal from the IR thermometer is converted by equation

$$y = 59.76467 \cdot x + 0.45244, \tag{27}$$

where y is the temperature in Celsius and x the voltage signal from the IR thermometer. The equation was acquired by making a linear fit to the calibrated values in the manual of the IR thermometer. The fit is shown in figure 17.

Digital signal acquisition is shown in figure 18. Pulses are counted up from 0 and the falling edge of the square wave.

Calculation of RPM is shown in figure 19. The number of pulses recorded in the previous cycle of the while loop is subtracted from the number of pulses recorded in the current loop. The resulting number of pulses is divided by 128 which is the number of pulses in one 360° rotation. The optical encoder is connected to the electric motor which rotates the lower sample through a set of gears. The gear ratio is 11 which is taken into account in the program. In addition to RPM the total number of pulses is counted as well as total number of revolutions.

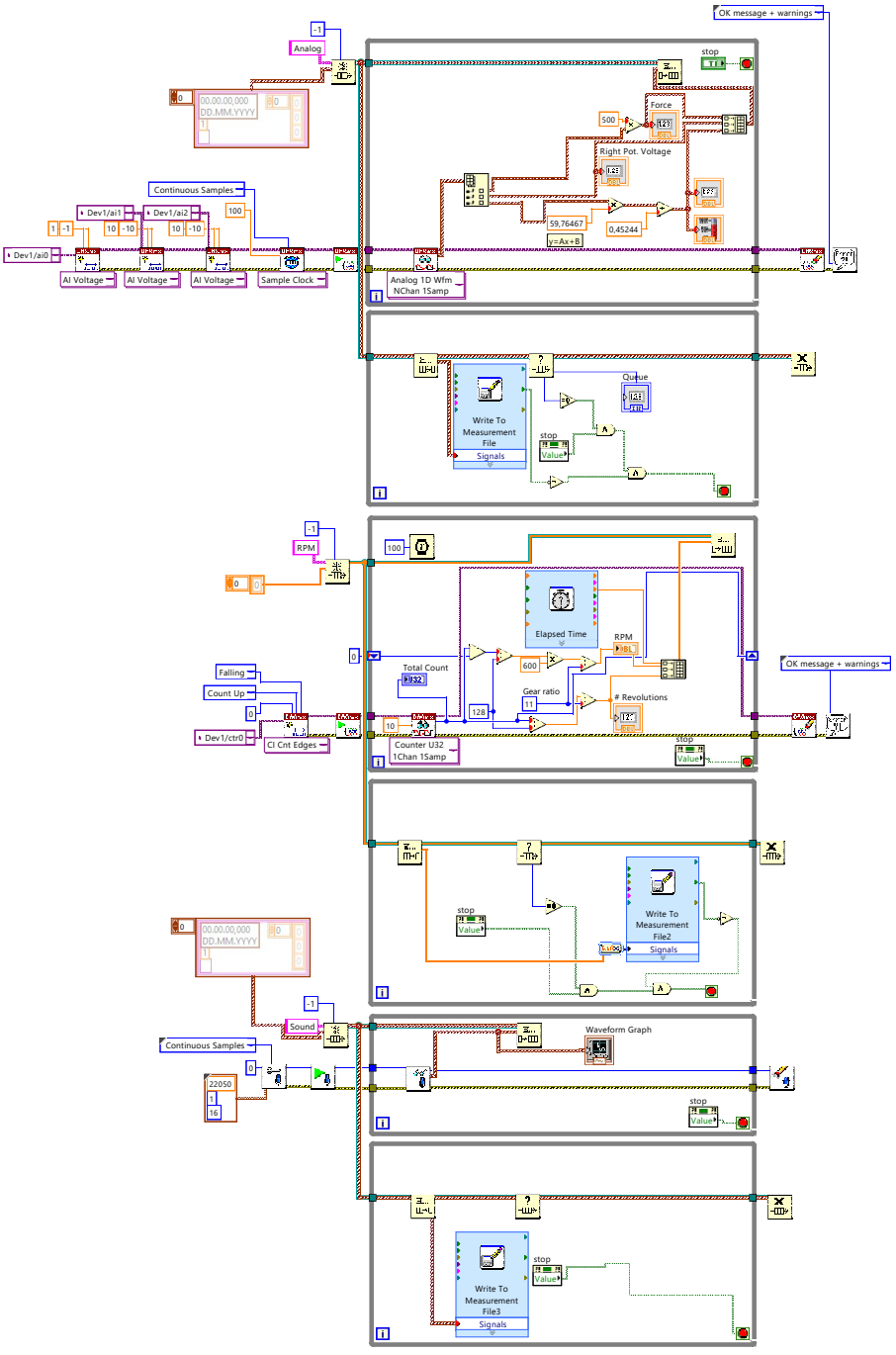

Figure 14. *Full measurement program.*

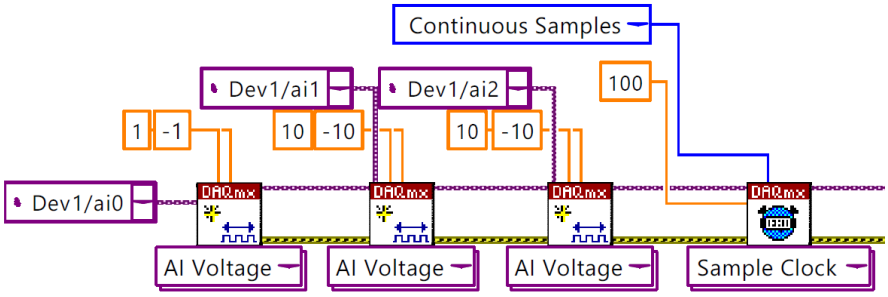

Figure 15. *Analog data acquisition settings.*

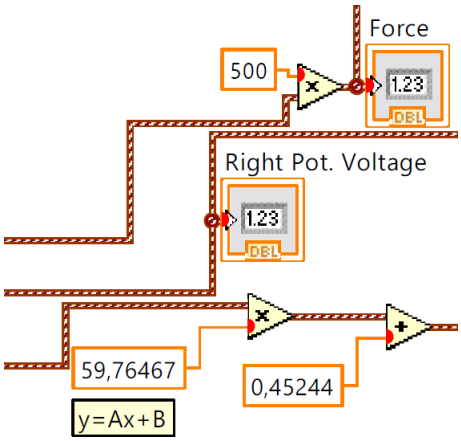

Figure 16. *Analog signals converted into physical quantities.*

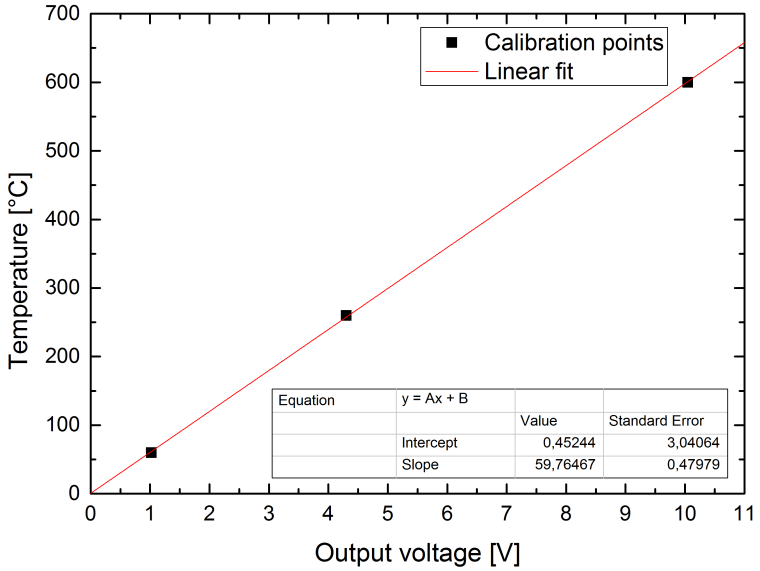

Figure 17. *Calibration of the IR thermometer.*

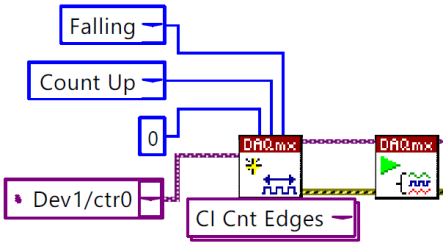

Figure 18. *Digital signal acquisition settings.*

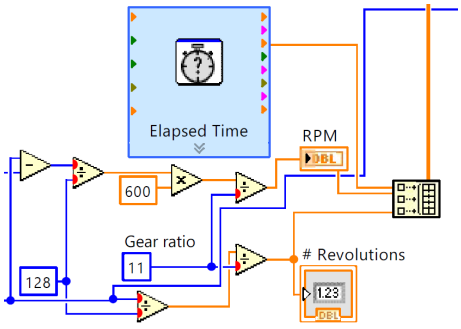

Figure 19. *Calculation of RPM.*

3.2 Sample Preparation

The sample precursors were drill core samples of veined gneiss from Olkiluoto with an approximate diameter of 42 or 45 millimetres. The total length of the samples varied by drill core. In order to fit them in the apparatus they were cut to the appropriate length during preparation. The original surfaces of the drill cores were smooth and their diameters large. A large diameter results a lower compressive pressure. Therefore a method to produce uniformly rough surfaces while reducing the diameter of the surfaces was required. This method is presented in chapter 3.2.1. In addition to rough samples, smooth samples were ground to study the instance of no wear particles. The preparation of smooth samples is presented in chapter 3.2.2. The cutter used to manufacture the samples is showed in figure 20.

3.2.1 Rough Surfaces

Producing samples with surfaces that have uniform roughness is challenging. Cutting disc leaves a flat surface and modifying the surface after cutting is difficult. Figure 21 shows the process of cutting the samples. In order to achieve natural but uniform roughness a shallow cut was made around the sample. Placing a wedge to the cut and hitting it with a hammer splits the sample into two parts. The resulting surfaces in most cases were natural with nearly uniform surface features. Since the splitting process is unpredictable some of the samples were unusable due to undesirable surface features. For example, individual pits and peaks spanning throughout the sample might be the most dominating features affecting the measured changes in force. Another undesirable feature is diagonal surfaces since they cause excess vertical displacement while rotating.

To achieve a high compressive pressure the area of contact has to be reduced. A peak was produced by making multiple adjacent disc-wide cuts to the other half of the split sample. This method preserves the surface features gained from splitting but the area of contact is significantly reduced. Smallest peaks produced were approximately 10 mm in diameter.

A rough surfaced sample ready for grinding is shown in figure 22. The left rock is the upper part of the sample and the right is the lower part. A paper collar is attached to the lower sample to prevent the ground particles from escaping the surface.

Figure 20. *The cutter used to manufacture the samples.*

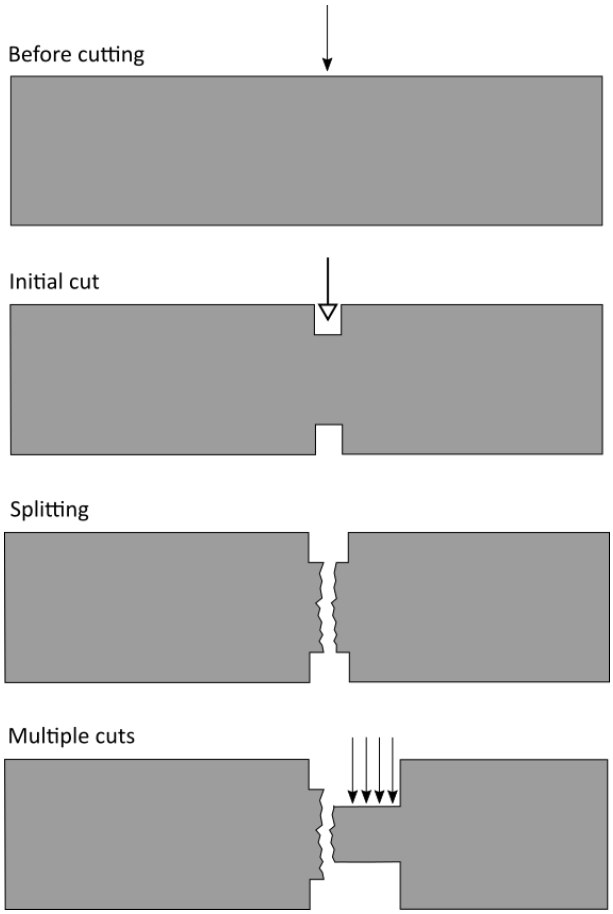

Figure 21. *Cutting of drill core samples. Black-headed arrows show points of cutting. The white-headed arrow shows the point of applied force to split the sample into two parts.*

Figure 22. *Rough surfaced samples. Upper sample is on the left and the lower is on the right.*

3.2.2 Smooth Surfaces

To study the instance of no wear particles smooth surfaces were required. The drill cores' ends readily had smoother surfaces than the cutter in figure 20 can produce. Therefore the cutter was used only to cut the drill cores to the appropriate length. A smooth surfaced sample is shown in figure 23. It can be seen from the photograph that the surface is not perfectly smooth but instead some scratches exist.

Figure 23. *A smooth surfaced sample.*

4 Results and Discussion

A total of 33 samples were ground. Samples number 1–25 were rough surfaced, differing in diameter, and ground under the same normal force, i.e. same amount of weights on the platform. Samples number 28–31 were rough surfaced but ground under constant normal pressure. Smooth surfaced samples numbered 26a–26d and 27, 32, and 33 were ground under varying normal force. All samples are listed in table A.1 in appendix A. Error calculations are presented in appendix B [29]. Results are presented in appendices C and D.

The samples are categorized as A, B, C, or D (black, grey, red, and white) depending on their appearance. Samples from each category before and after grinding are shown in figures 24, 25, 26, and 27. In each sample the peak was worn and smoothed by the grinding. The lower samples have a crater of grains on their surface formed by particles from both upper and lower samples.

Figure 24. *Category A sample before and after grinding (sample 22).*

Figure 25. *Category B sample before and after grinding (sample 9).*

Figure 26. *Category C sample before and after grinding (sample 19).*

Figure 27. *Category D sample before and after grinding (sample 11).*

4.1 Constant Normal Force

Samples 1–25 were ground under constant normal force, i.e. the same amount of weights. Total mass loaded on top of the sample including the platform itself was 173.99 kg. Target amount of rotations was 72 which translates into 12 minutes with a rotation speed of 6 rpm. The rotation speed commonly fluctuates from 5 to 7 rpm during grinding. Therefore the number of rotations was used as the stopping mark. The target was chosen in such a way that all significant changes in friction were included in the data while keeping the time required for a single measurement practical.

4.1.1 Increased Area of Contact

The grinding process creates a crater of grains on the lower sample's surface. Since the peaks of each sample have different areas they were worn out at different times. If the peak was completely worn off and the area of contact increased the edges of the crater were flattened. Figure 28 shows crater edges of sample 25 flattened by contact with the upper surface. Some of the smaller peaks were worn out completely, and therefore the area of contact increased during the measurement. The time of change was visually observed and marked down for later reference. Peaks of samples 13, 17, 23, 24, and 25 were worn out before the grinding ended. For each sample the data after the change in area of contact was disregarded. Figure 29 shows the changes in temperature and friction coefficient during the grinding of sample 23. The data is averaged every 10 s. The peak was worn completely off before 100 s and after it both friction coefficient and temperature increased sharply. The temperature increase is observed after the rise in friction coefficient because heat conduction to the surface does not occur instantly.

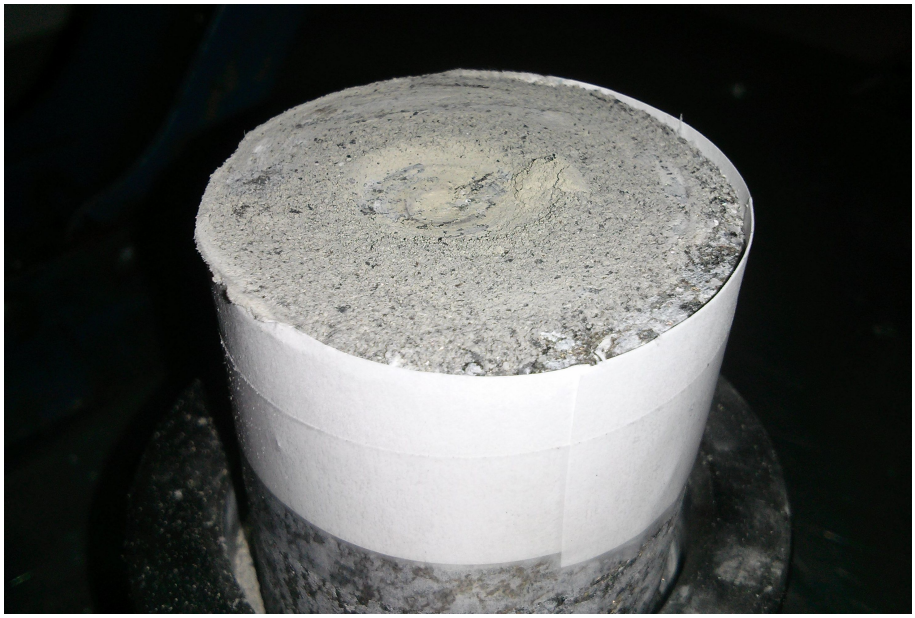

Figure 28. *Flattened crater of sample 25 caused by full contact with the upper sample part.*

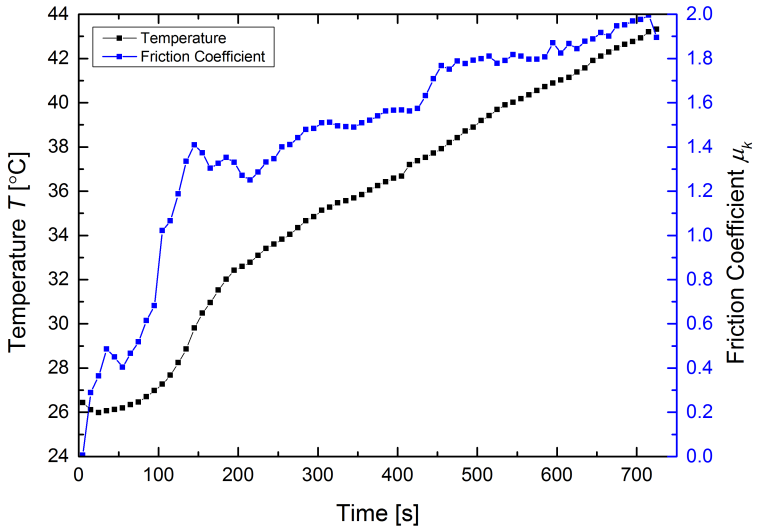

Figure 29. *Temperature and friction coefficient during the grinding of sample 23. Data averaged every 10 s.*

4.1.2 Unsuccessful Measurements

During the grinding of samples 5, 15, and 18 undesirable effects were observed. Therefore they are excluded from the results and marked red in the appendices. Sample 5 had a plastic collar instead of a paper one which was ground against the rock surface resulting in anomalous results (fig. 30). Sample 15 was cracked from the bottom of the lower part near the fixing screws and sample 18 turned at an angle during grinding.

Figure 30. *Black plastic collar ground against the surface of the upper rock sample.*

4.1.3 Torque and Friction Coefficient

Samples 1–25 were ground under constant normal force. Torque and friction coefficient are presented as a function of time for samples 1–25 in appendix D. The data was averaged every 10 s which is once per rotation at approximately 6 rpm. Torque and friction coefficient of sample 11 are shown in figure 31. The friction coefficient is identical to the torque since τ is the only variable in equation 24 if grinding is conducted under constant normal force. When comparing multiple measurements with each other the diameter of the peak d and mass M become additional variables. Category of the sample is a variable if comparing different rock types with each other.

The anomalously high or low values in the beginning or the end of the data are caused by the measurement program being started or stopped. Commonly the measurement program was started before lowering the upper sample into contact. Therefore the measured force is 0 in the beginning.

Torque and friction coefficient fluctuate during the grinding process periodically. Figure 32 shows how the fluctuations of friction coefficient correlate with vertical displacement. The samples' surfaces cannot be perfectly uniform. Small pits and peaks on the surface cause the displacement.

The weight platform is floating on three rails and the displacement causes it to rock from side to side. The potentiometer is attached to one of the rails, and therefore the rocking effect is amplified. In figure 33 the position of sample 11 is averaged every 10 s which cancels out most of the rocking effect. The position is significantly decreased in the beginning of the measurement because the upper sample is first lowered into contact. During the grinding the peak is slowly worn off and the position decreases.

The time dependent data showed no signs of distinguishable processes but the general level of the measured quantities was different for each sample. Therefore the comparison was conducted through mean values of the measured quantities. Mean torque τ and mean friction coefficient μ_k of samples 1–25 are presented as functions of compression pressure P in figures 34 and 36. Samples 5, 15, an 18 are excluded from the results.

Equation 24 has the same principle quantities as the basic equation for kinetic friction. Hence torque can be thought to be analogous with friction force. Torque shows signs of decaying exponential dependency on pressure. Mean torque decreases as the pressure

increases. On higher pressures torque seems to saturate to a certain level while on low pressures it increases sharply. Corresponding behaviour has also been observed in computer simulations [30]. Category of the sample has negligible effect but grey samples appear to follow the exponential decay more reliably.

Figure 35 shows the relative frequency of torque for samples 3, 4, and 6–9. Samples are arranged from the lowest pressure to the highest. Highest concentration of counts are found around the calculated mean torque of each sample. The same inverse dependency on pressure can be seen as the stacks move towards 0 Nm when pressure increases.

Amontons' 2nd law stated that friction force is not dependent on the area of contact. Under constant normal force pressure is only affected by the peak diameter, i.e. area, which indicates that in this instance the friction force is indeed affected by the area of contact. The observed behaviour might be explained by the formation of wear particles which is enhanced on higher pressures. On lower pressures all asperities might not fragment and form wear particles or the particles might not be ground small enough to decrease friction. In addition the wear particles might be more densely packed under high pressure.

Mean friction coefficient as a function of pressure is shown in figure 36. Order of the samples is similar to figure 34 but no clear dependency is visible. Friction coefficient is independent of the pressure and might be only affected by the physical surface properties of each sample. The diameter of the peak becomes an additional variable when comparing friction coefficients of different samples under constant normal force. Therefore the scattering of mean values is different when comparing torque and friction coefficient. Since the normal force is constant pressure depends only on the area of contact, i.e. peak diameter. Plotting the friction coefficient as a function of peak diameter results in an inverted order of the data points (fig. 37).

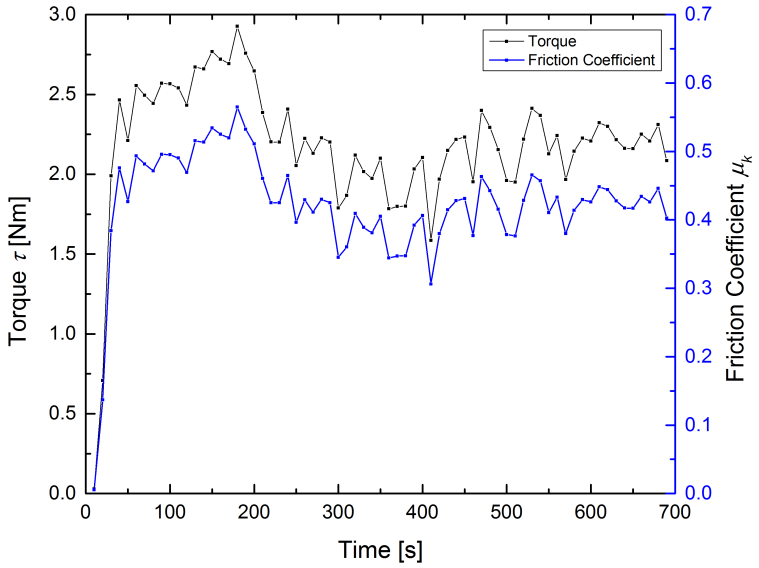

Figure 31. *Torque and friction coefficient of sample 11 as a function of time. Averaged every 10 s.*

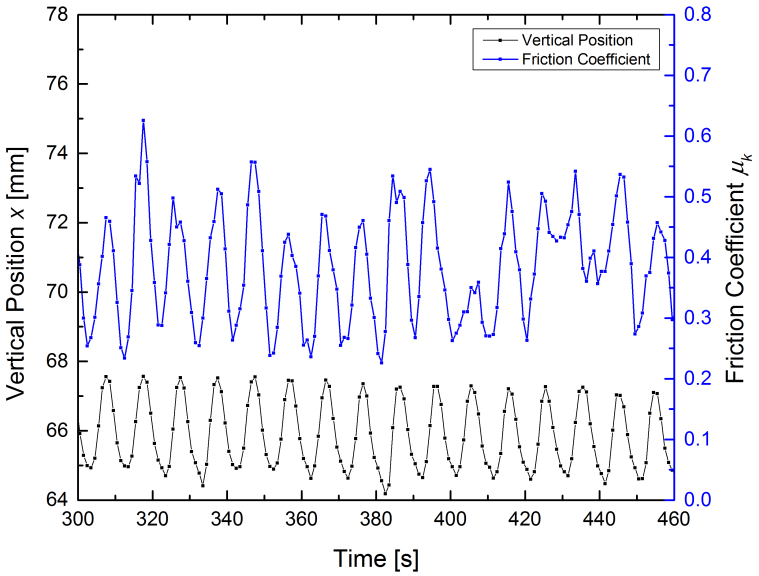

Figure 32. *Friction coefficient and vertical position of sample 11. Averaged every 1 s.*

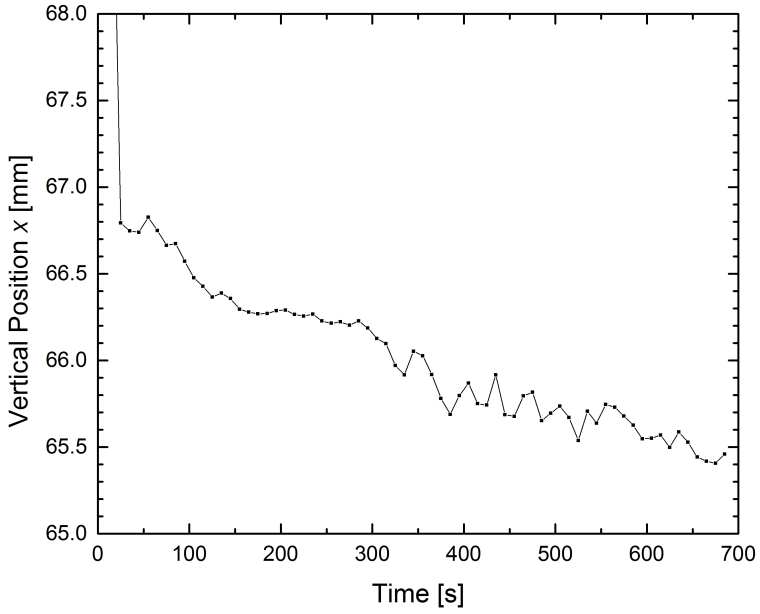

Figure 33. *Vertical position of sample 11. Averaged every 10 s.*

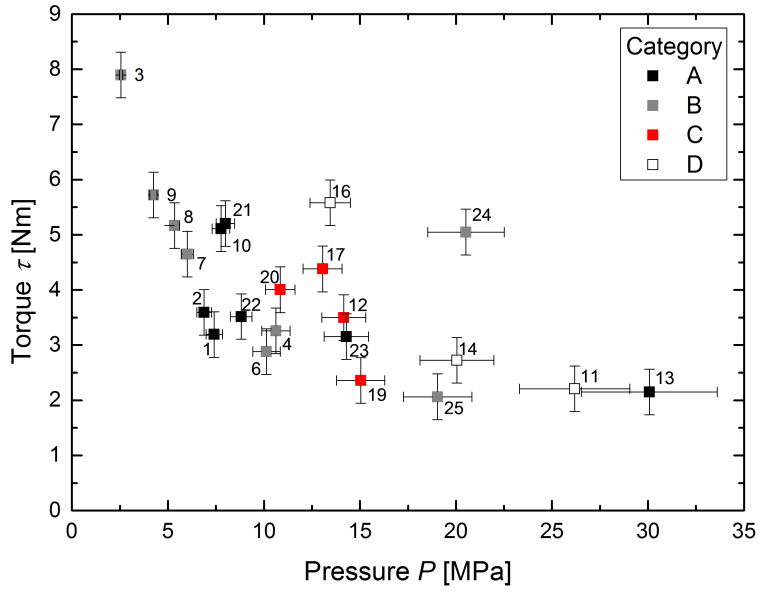

Figure 34. *Mean torque as a function of pressure under a constant normal force.*

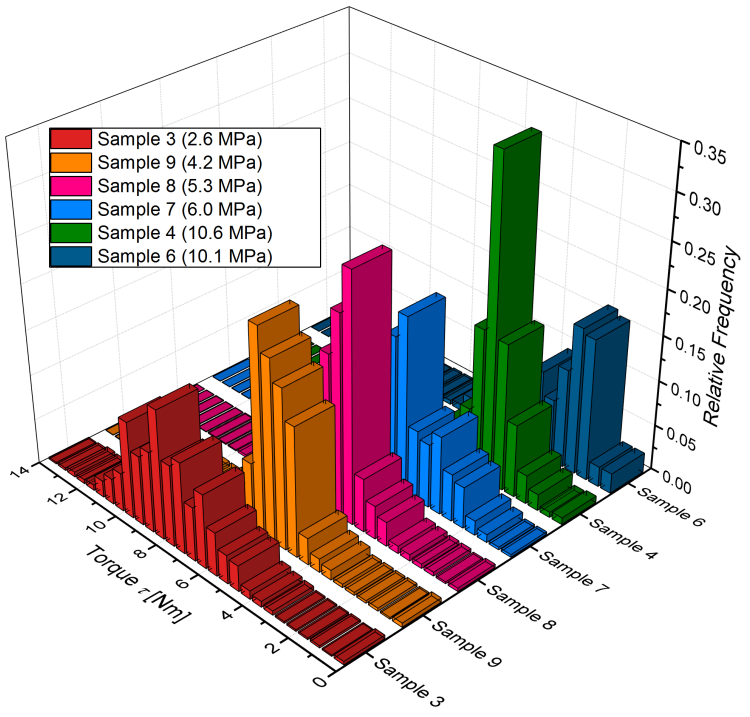

Figure 35. *Relative frequency of torque under a constant normal force. Bin size 0.5.*

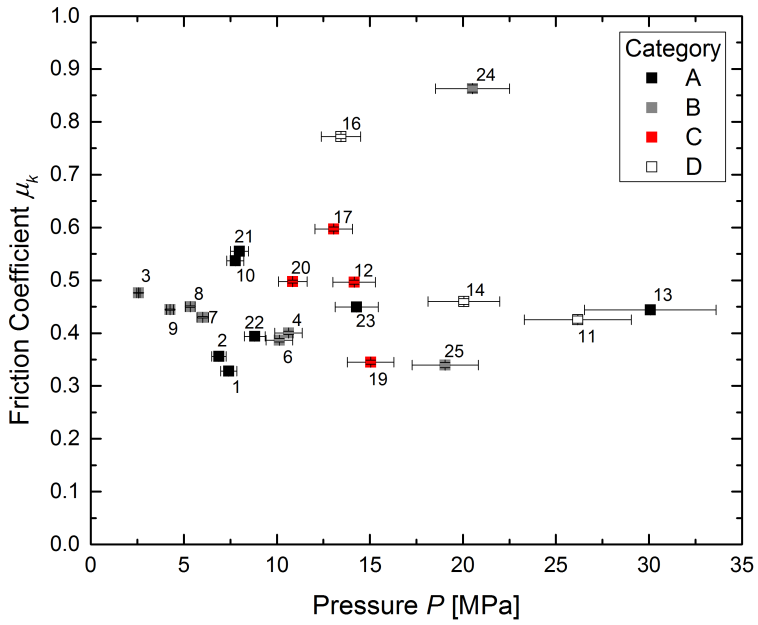

Figure 36. *Mean friction coefficient as a function of pressure under a constant normal force.*

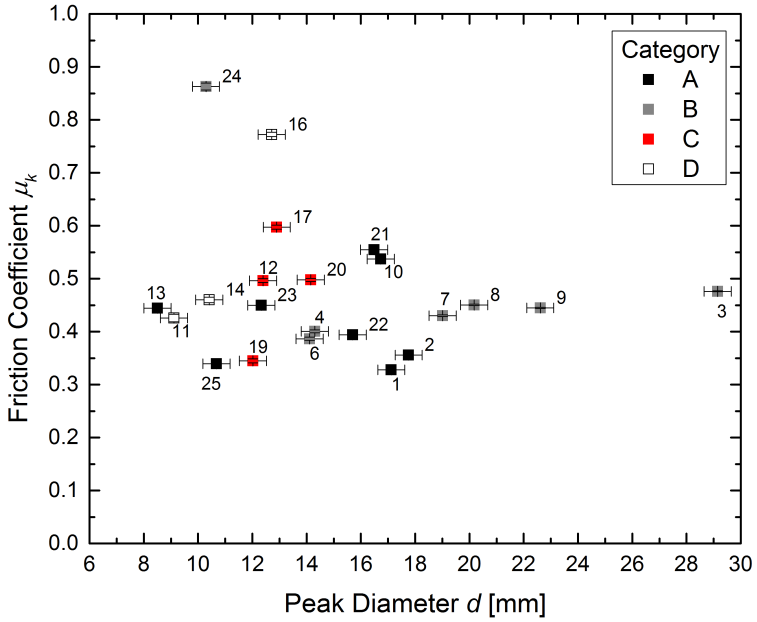

Figure 37. *Mean friction coefficient as a function of peak diameter under a constant normal force.*

4.1.4 Temperature and Vertical Displacement

During grinding the temperature of the rock surface increased. Temperature increase of sample 11 is shown in figure 38 as an example. Data for sample 24 was disregarded due to problems with the IR thermometer. The sensor was in contact with the aluminium mount during measurement which caused it to output anomalously high values.

Calculating the difference between maximum and minimum temperature, i.e. ΔT, enables comparison between all the samples. Temperature change of each sample as a function of pressure is shown in figure 39. The magnitude of change is high on lower pressures but as the pressure increases the observed change in temperature is lower. Torque was lower on high pressures and as a result the generated frictional heat is lower. The temperature change is inversely dependent on the pressure. If plotted against peak diameter (fig. 40) the dependency is direct as per the equation of pressure B.1.

Previously in figure 34 torque showed inverse dependency in pressure. Temperature change as a function of torque is shown in figure 41. Torque was inversely dependent on pressure as was temperature change which results in direct dependency between torque and temperature.

Temperature change as a function of friction coefficient is shown in figure 42. The magnitude of temperature change seems not to be dependent on the coefficient of friction. The dimensionless coefficient represents the ratio of friction force and normal force. Therefore it is conceivable that both the coefficient of friction and the temperature change are the product of those quantities rather than the cause of them. The generation of frictional heat is therefore the result of the friction force itself which is affected by compressive normal pressure. Samples 16 and 17 are outside of the main group of data points since their mean friction coefficient is among the highest of all samples.

Measurement of vertical displacement proved to be problematic as explained in chapter 4.1.3. In addition to the problems explained previously the measurement system had one fundamental flaw rendering most of the potentiometer data unusable. Same 24 V power source was used for the IR thermometer and the potentiometer. The maximum input voltage of the potentiometer is 10 V. If the position was over a certain limit the output of the sensor was constantly 10 V. Data from measurements occurring under the 10 V limit are shown in figure 43.

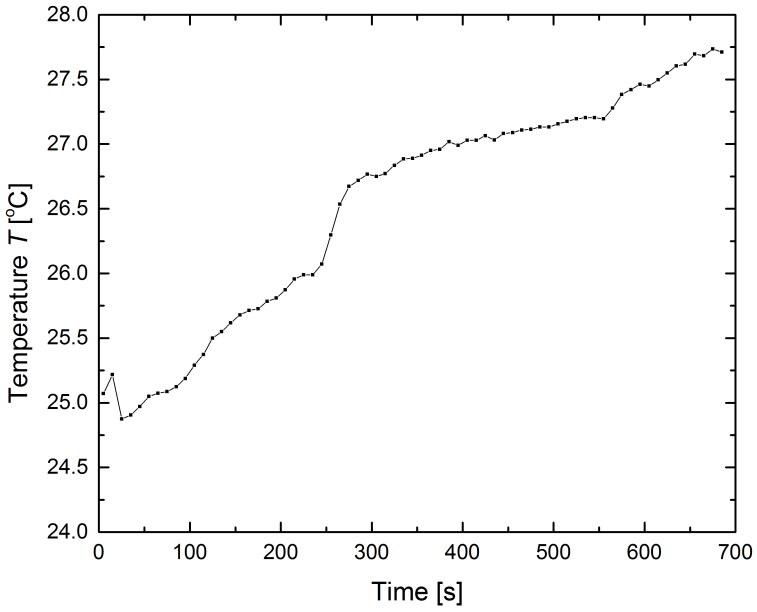

Figure 38. *Temperature of sample 11. Averaged every 10 s.*

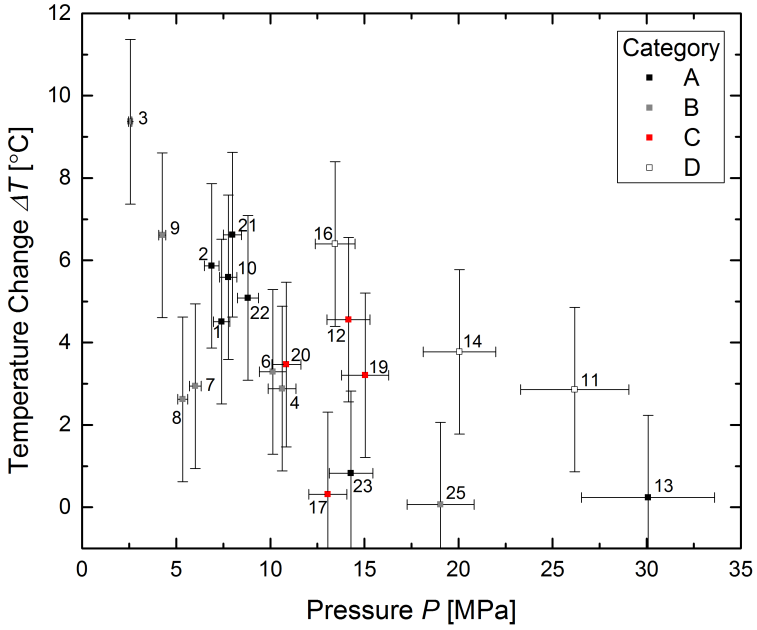

Figure 39. *Temperature change as a function of pressure under a constant normal force.*

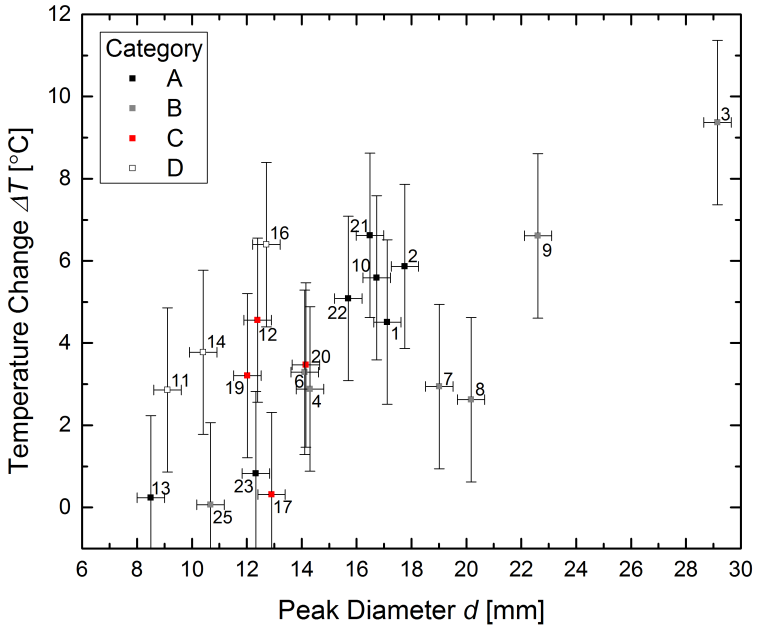

Figure 40. *Temperature change as a function of peak diameter a constant normal force.*

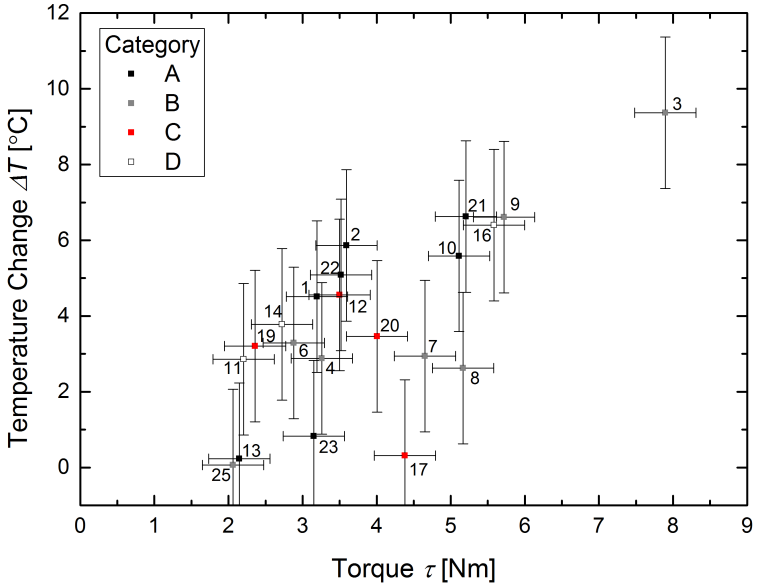

Figure 41. *Temperature change as a function of torque under a constant normal force.*

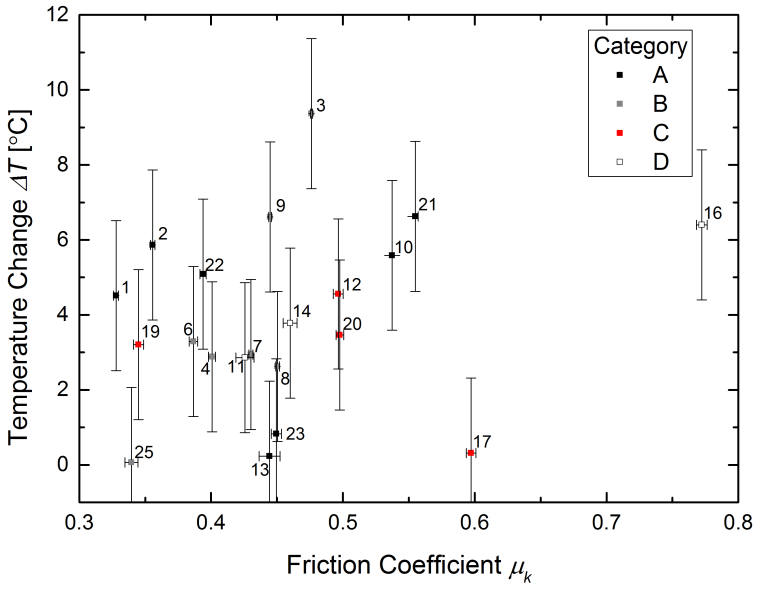

Figure 42. *Temperature change as a function of friction coefficient under a constant normal force.*

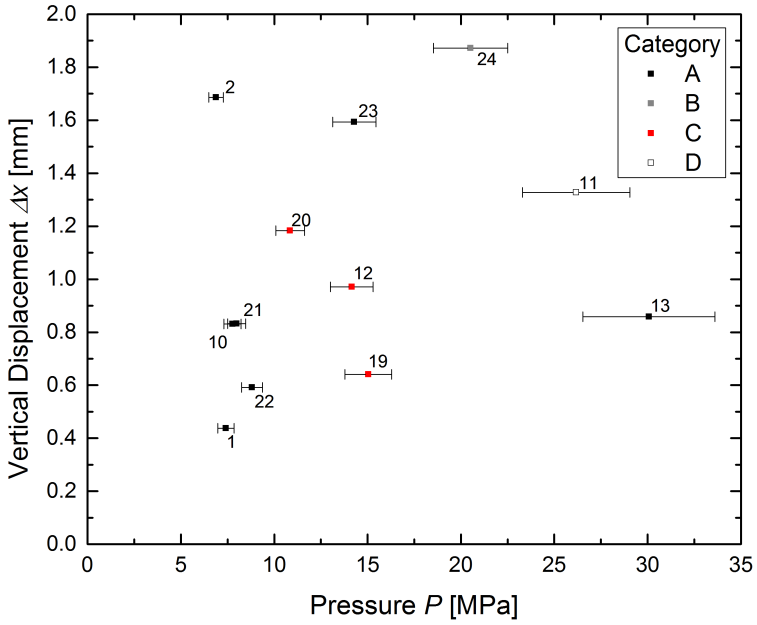

Figure 43. *Vertical displacement as a function of pressure under a constant normal force.*

4.2 Constant Normal Pressure

Measurements were carried out under constant normal pressure by changing the area of the peak and the mass loaded on the platform. Pressure was kept at approximately 2.5 MPa. Figures 44 and 45 show the behaviour of torque under constant pressure. When pressure is constant both the loaded mass and the diameter of the peak seem to directly affect the observed torque. In this instance both seem to affect the torque but on the basis of the results in chapter 4.1 it is feasible that the peak diameter is the more important quantity. Previously in the instance of constant normal force the peak diameter was the dominant quantity.

Figures 46 and 47 show friction coefficient as a function of mass and diameter, respectively. Again, in contrast to torque, friction coefficient appears to have no dependency on either and it remains fairly constant. Similar behaviour of friction coefficient and peak diameter was observed when grinding was conducted under constant normal force (fig. 37). Possibly the friction coefficient is only affected by the surface roughness of the sample since it is independent of the grinding parameters, such as mass and peak diameter. The small differences in the friction coefficient of samples 28–31 are caused by the uniqueness of the surfaces and the slight differences in normal pressure.

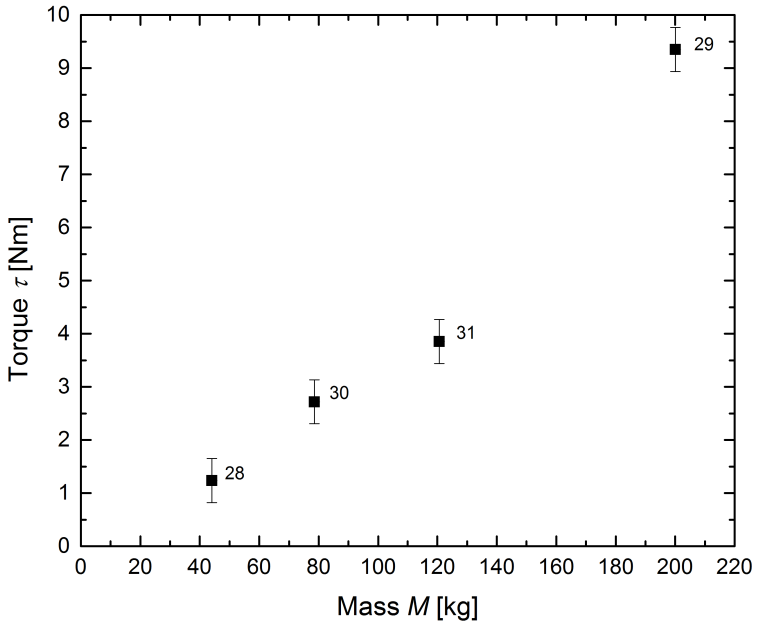

Figure 44. *Mean torque as a function of mass under a constant pressure.*

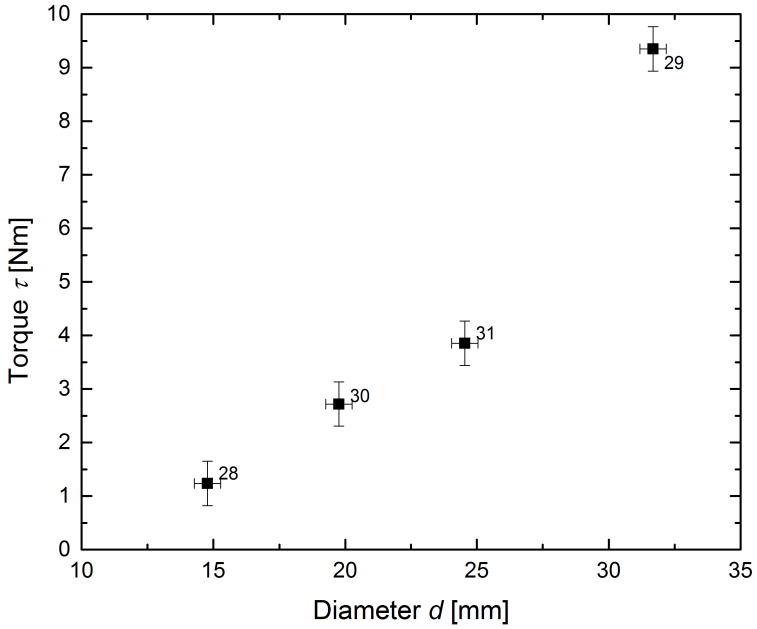

Figure 45. *Mean torque as a function of peak diameter under a constant pressure.*

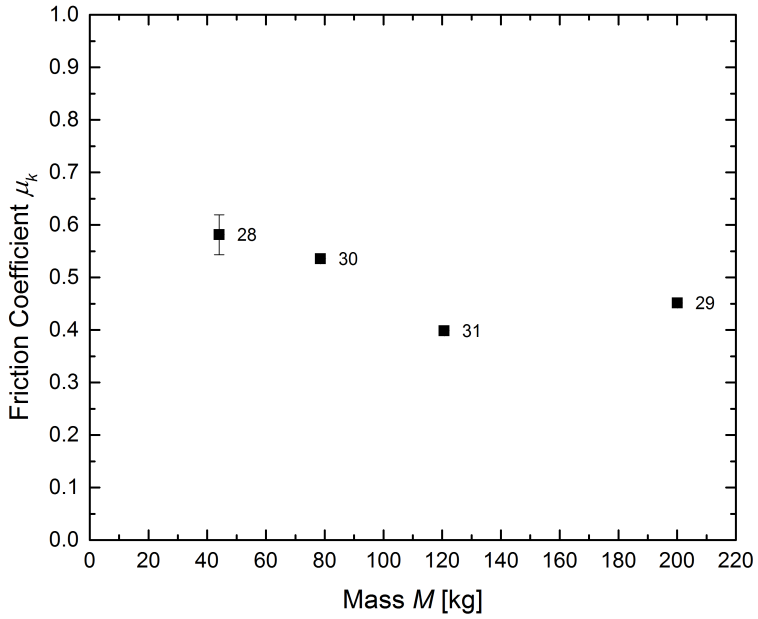

Figure 46. *Mean friction coefficient as a function of mass under a constant pressure.*

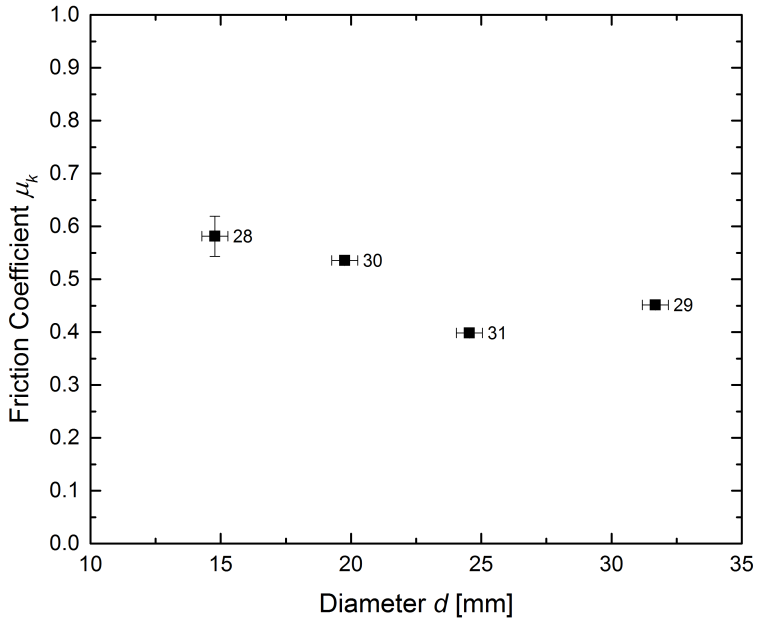

Figure 47. *Mean friction coefficient as a function of peak diameter under a constant pressure.*

4.3 Smooth Surface Samples

Two different methods were used to grind smooth surfaced samples. Grinds 26a–26d are in fact the same drill core ground consecutively. The amount of loaded mass was decreased after each measurement. Samples 27, 32, and 33 were unique drill cores with surfaces cut from the ends of a drill core ground under constant loaded mass, i.e. under constant pressure.

Mean torque and mean friction coefficient of smooth surfaced samples are presented in figures 48 and 49 as a function of pressure. Blue data points represent sample 26 ground with the same surface consecutively while black points represent the unique smooth surfaces.

Grinding the same surface polishes it and as a result both mean torque and mean friction coefficient decrease from 26a through 26d. Combined with decreased loaded mass after each measurement the change is amplified. Grinds 26a–26d could be regarded as a single measurement rather than a set of different measurements due to the continued grinding. From that point of view torque increases as pressure increases if the loaded mass is disregarded. Grinding the same surface was not a working method to study smooth surfaces since the previous grind always affects the next one due to polishing.

Samples 27, 32, and 33 have almost identical diameters and identical grinding conditions but torque and friction coefficients differ from each other. Therefore the differences arise from the surfaces themselves. Although the surfaces were smooth to the hand some roughness still exists. While the measured values are not perfectly identical they are reasonably similar to confirm that consistent results can be gained. The mean torque and friction coefficients are high even though minimal grinding occurs with smooth samples. Similar results were observed by Mora and Place who calculated that the lack of gouge results a higher average friction in a fault [12].

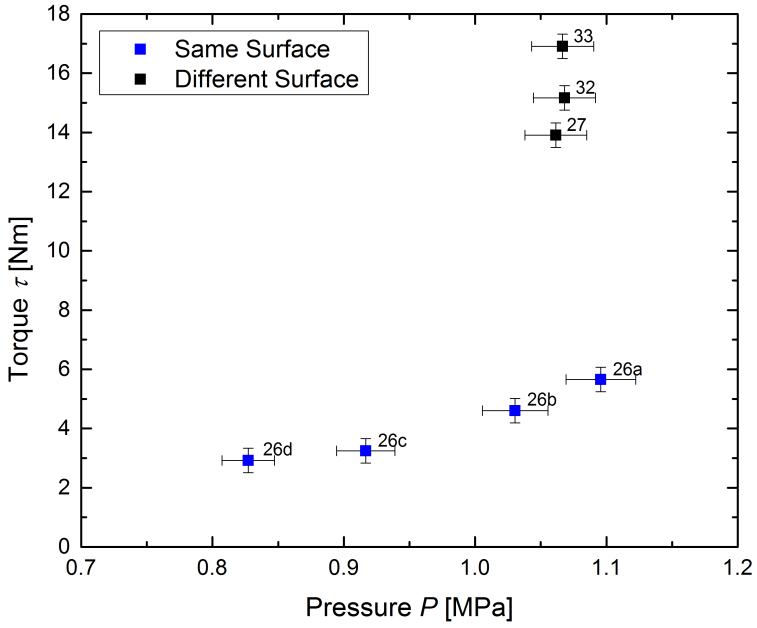

Figure 48. *Smooth surface samples. Mean torque as a function of pressure.*

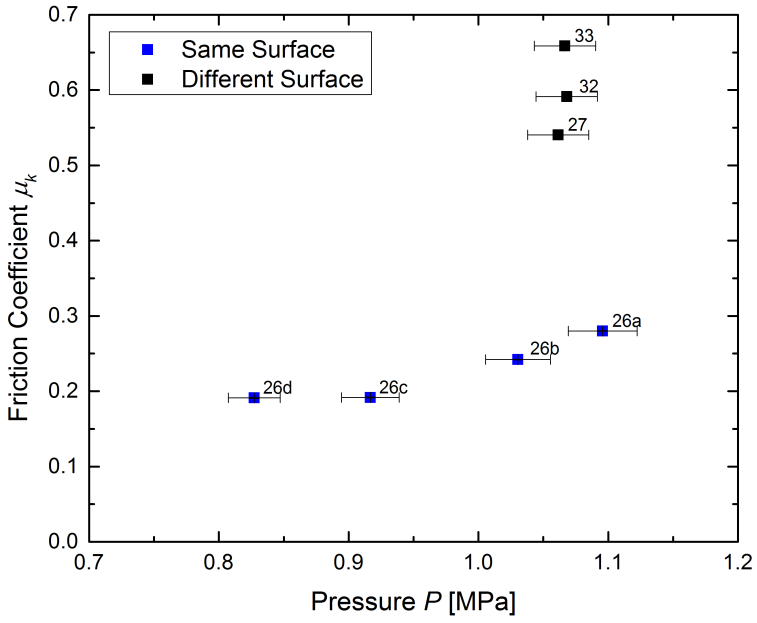

Figure 49. *Smooth surface samples. Mean friction coefficient as a function of pressure.*

4.4 X-ray Microtomograghy

Xradia MicroXCT-400 microtomograph was used to image the ground particles of sample 11 at a resolution of 0.59 μm/pixel. Grains were collected from two different areas of the surface. Finer grains were from the middle of the crater and more coarse grains were from the edges outside surface contact. Figure 50 visualises the areas of sample collection.

Slices of coarse and fine grains are shown in figure 51. The grains are angularly shaped and perfectly spherical wear particles are not present in the samples within the used image resolution. The degree of angularity varies. The shape varies from sharp elongated particles to more angular round particles. The torque was found to be inversely dependent on pressure and the mean torque of sample 11 was among the lowest measured. Regardless of the shape of the particles the friction force is lower if the pressure is high. Spherical particles could decrease the friction further but they were not formed during grinding. Possibly grinding the sample considerably longer could produce more rounded out wear particles.

The grains in the middle have been ground for a longer time than the grains from the crater edges which are outside the area of contact. Rotational forces cause the grains to migrate from the center of the area towards the edges and eventually outside of the area in contact. Size distribution in figure 52 confirms that the grains collected from the middle of the crater are finer than the ones from the edges. Over 70 % of the fine grains are 50 μm^3 or smaller. Only 30 % of the coarse grains are 50 μm^3 or smaller. Quantity of particles over 50 μm^3 is higher in the coarse sample.

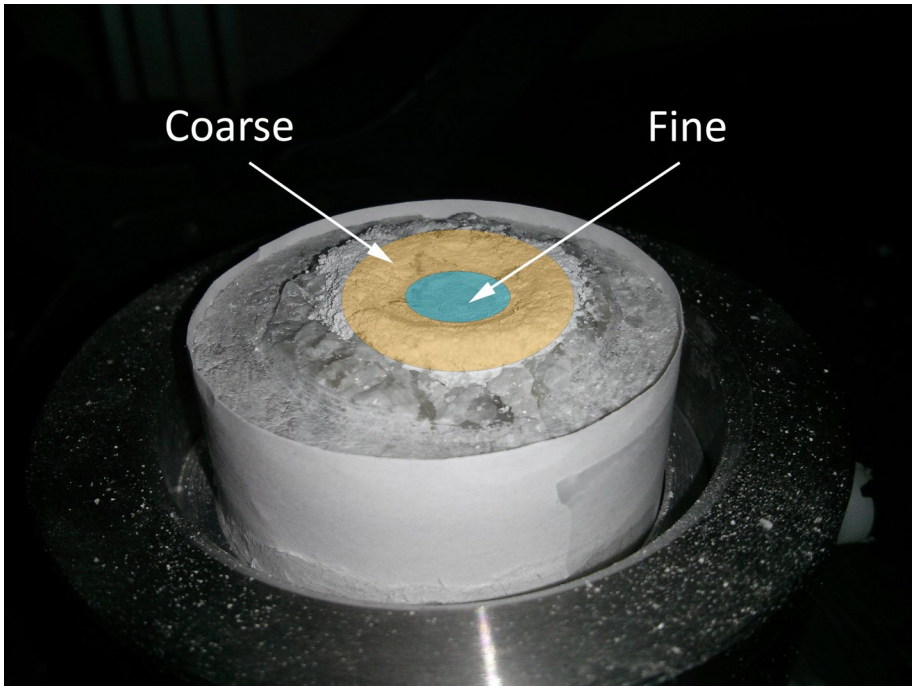

Figure 50. *Sample 11 after grinding. Fine grains were collected from the blue area. Coarse grains were collected from the orange area.*

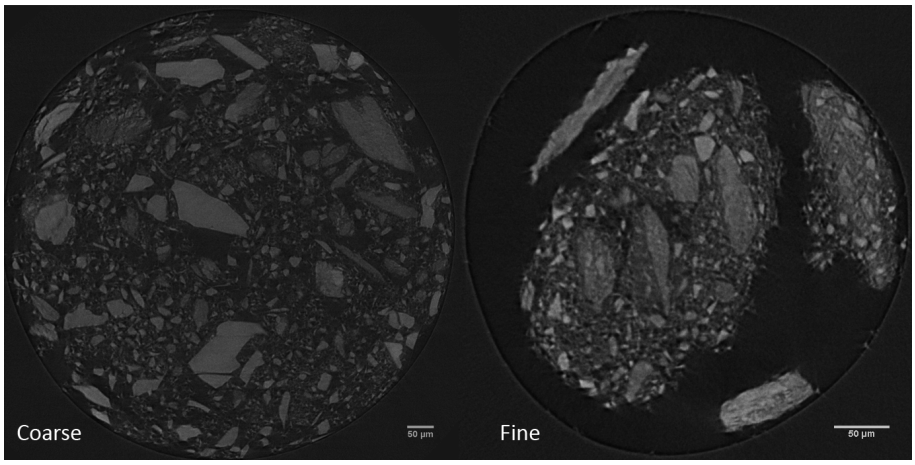

Figure 51. *Slices of coarse and fine grains of sample 11.*

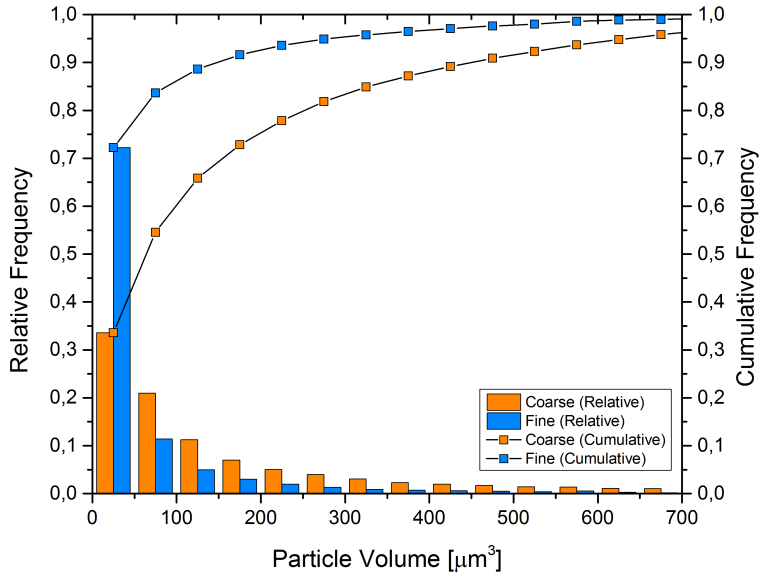

Figure 52. *Size distribution of fine and coarse grains in sample 11.*

4.5 Improvement Ideas

Carrying out new and experimental measurements requires continuous improvement. Stonegrinder has provided useful data but further refinement of the techniques is necessary. This chapter introduces improvement suggestions to the equipment and the grinding process.

Sample preparation is currently based on random chance. When the drill core is split in two the result cannot be predicted. The initial cut could be made deeper to reduce the thickness of the drill core even further. This would reduce the chance of receiving unusable surfaces because the crack has a shorter distance to propagate. A completely reliable way of producing rough surfaces might not be possible. The peak for the sample was produced by making multiple disc-wide cuts next to each other. The cutter has a guide to keep the sample straight but the depth of the cut has to be approximated by hand. A guide to stop the sample from being cut too deep would ease the process.

Stonegrinder had sensor problems which made some of the data unusable. The potentiometer requires a separate 10 V power source to prevent over voltage. The output of the IR thermometer is unreliable if it is in contact with a metal surface. Better insulation of the probe and recalibration would improve the reliability. Considering the ground samples more tests could be performed on them. Weighting the grains could provide the volume of wear and imaging a cleaned ground surface might reveal the cavities or scratches made by the grains. This could possible lead to determine the type of wear occurring which again could be used to refine the equation of friction coefficient.

Audio data was not discussed in the results because handling it proved to be problematic. Sampling rate of audio is high and the measurement program is strained due to the large amount of data being saved. In addition the file size of the audio was large which made the analysis and compiling of the results slow. Initial analysis of sound pressure from a couple of samples did not reveal anything ground breaking and for this reason further study was abandoned. If audio recording is continued the measurement program needs to be improved or an external software could be used. Preferably the audio should be readily saved as a waveform file.

5 Conclusions

Discovering a plausible explanation for the lack of frictional heat along fault planes is the main purpose of this research. The main hypothesis was that fragmented particles from the surface would form a system of rounded grains acting as ball-bearings. Therefore the friction between the surfaces would decrease thus reducing the generated frictional heat. To test the hypothesis in practice a unique apparatus was designed.

Stonegrinder was built to measure friction between two drill core samples. The samples were different types of gneiss varying in color and composition categorized as A, B, C, or D. Category A samples were dark and layered migmatitic gneisses. Category B samples were grey and strongly migmatized with no visible layers. Category C and D samples were red coarse-grained and light quartz-rich gneisses, respectively.

Rough surfaced samples were produced by first cutting a small incision to the drill core and then splitting it in two by force. Splitting the sample produced a rough surface but occasionally the created surface was excessively diagonal, and therefore unusable. Smooth surfaces were cut from the ends of the drill cores. The rough surface samples were ground under two different conditions: constant normal force, and constant normal pressure. Smooth surface samples were ground under constant normal force and pressure.

During the grinding process problems were encountered with some of the samples. Samples that were excluded from the results had turned at an angle or cracked from near the fixing crews. A different type of problem occurred with samples having a narrow peak. The grinding time was fixed for all the samples but some of the peaks were completely worn off before stopping the measurement. If the peak wears off the area of contact increases. The time of wearing off was marked down for the samples and the data after that point was disregarded in results.

The equation for the coefficient of friction has three variables, torque τ, peak diameter d, and mass M. Considering a single sample torque and friction coefficient fluctuate identically because d and M are constant. However comparing samples with each other turns d and M into variables unique to each sample. Classical models were used to derive the equation for the coefficient of friction. Therefore torque is regarded to be analogous with friction force.

The comparison of the samples was carried out through the mean values of torque and friction coefficient. Torque was found out to be inversely dependent on pressure with signs of exponential decay under constant normal force. According to Amontons' 2nd law friction should be independent of the area of contact but in this instance the law does not apply. Under constant normal force pressure is dependent only on the peak diameter, i.e. area of contact. Possibly a higher pressure creates more wear particles and wears off surface asperities which causes a decrease in observed friction. The magnitude of temperature change was considerably lower for samples ground under high pressure which also indicates decreased friction. Mean friction coefficients under constant normal force showed no signs of dependency on pressure or magnitude of temperature change.

Under constant normal pressure mean torque was directly dependent on peak diameter and loaded mass. Previously in the instance of constant normal force, changing the peak diameter had the most significant effect on torque. This indicates that the peak diameter is the dominant parameter also in this case. Similarly to measurements under constant normal force the friction coefficient was not dependent on peak diameter. In addition the loaded mass does not seem to affect friction coefficient either. The observed coefficient of friction was fairly constant through all measurements. The slight differences in the friction coefficients were caused by differing surface features and compressive pressures. Since friction coefficient was independent of the grinding parameters, such as mass and peak diameter, surface roughness is the probable cause for different friction coefficients.

Smooth surfaced samples shared similar values of mean torque and friction coefficients because grinding conditions were set to be nearly identical. Consistent results confirm that the apparatus performs reliably. The smooth samples had higher values of mean torque and friction coefficient than rough samples. The lack of wear particles increased friction.

The ground wear particles form a crater-shaped formation on the sample surface. Rotational forces cause the particles to migrate from the middle to the edges of the area of contact. From the edges the particles end up outside the grinding area and start to accumulate. Grains from the middle and from the accumulated crater edges were imaged with X-ray microtomography. The particles were angularly shaped and the expected perfectly spherical or even hexagonal particles were not found in significant amounts. Comparison of size distribution confirmed that the wear particles in the middle were smaller than the particles on the edges.

While spherical wear particles or the spontaneous formation of a system of ball-bearings were not discovered, friction force was found to be low on high pressures if some wear particles were present. Tectonic stresses across a fault can be considerably higher than those produced in the experiment. Therefore even lower friction might be achievable. Thus the results of the experiment support the view that fault gouge decreases friction and the generation of frictional heat.

References

[1] A. H. Lachenbruch and J. H. Sass. "Heat flow and energetics of the San Andreas Fault Zone". In: *Journal of Geophysical Research: Solid Earth* 85.B11 (1980), pp. 6185–6222. DOI: 10.1029/JB085iB11p06185.

[2] J. A. Åström and J. Timonen. "Spontaneous formation of densely packed shear bands of rotating fragments". In: *The European Physical Journal E* 35.5 (2012), pp. 1–5. DOI: 10.1140/epje/i2012-12040-y.

[3] B. Bhushan. *Introduction to Tribology*. 2nd ed. Tribology in Practice Series. Wiley, 2013. ISBN: 9781118403228.

[4] I. Svetlizky and J. Fineberg. "Classical shear cracks drive the onset of dry frictional motion". In: *Nature* 509 (2014), pp. 205–208. DOI: 10.1038/nature13202.

[5] R. W. Carpick and R. Bennewitz. "Friction: Let it slip". In: *Nature Physics* 10 (2014), pp. 410–411. DOI: 10.1038/nphys2985.

[6] P. Kearey, K. Klepeis, and F. Vine. *Global Tectonics*. 3rd ed. Wiley, 2009. ISBN: 9781444303223.

[7] M. Lehtinen, P. Nurmi, and T. Rämö. *Suomen kallioperä: 3000 vuosimiljoonaa*. Suomen Geologinen Seura ry., 1998. ISBN: 9529092601.

[8] E. M. Winkler. *Stone: Properties, Durability in Man's Environment*. 2nd ed. Springer-Verlag, 1975. ISBN: 9780387813134.

[9] T. Blenkinsop. *Deformation Microstructures and Mechanisms in Minerals and Rocks*. Springer, 2000. ISBN: 9780412734809.

[10] A. H. Lachenbruch and J. H. Sass. "Heat flow from Cajon Pass, fault strength, and tectonic implications". In: *Journal of Geophysical Research: Solid Earth* 97.B4 (1992), pp. 4995–5015. DOI: 10.1029/91JB01506.

[11] P. M. Fulton et al. "Low Coseismic Friction on the Tohoku-Oki Fault Determined from Temperature Measurements". In: *Science* 342.6163 (2013), pp. 1214–1217. DOI: 10.1126/science.1243641.

[12] P. Mora and D. Place. "Numerical simulation of earthquake faults with gouge: Toward a comprehensive explanation for the heat flow paradox". In: *Journal of Geophysical Research: Solid Earth* 103.B9 (1998), pp. 21067–21089. DOI: 10.1029/98JB01490.

[13] R. Heilbronner and N. Keulen. "Grain size and grain shape analysis of fault rocks". In: *Tectonophysics* 427.1–4 (2006). Deformation mechanisms, microstructure and

rheology of rocks in nature and experimentDeformation mechanisms, rheology and tectonics, pp. 199–216. DOI: 10.1016/j.tecto.2006.05.020.

[14] E. Rabinowicz. "The Formation of Spherical Wear Particles". In: *Wear* 42.1 (1977), pp. 149–156. DOI: 10.1016/0043-1648(77)90175-2.

[15] B.-D. So and D. A. Yuen. "Influences of temperature-dependent thermal conductivity on surface heat flow near major faults". In: *Geophysical Research Letters* 40.15 (2013), pp. 3868–3872. DOI: 10.1002/grl.50780.

[16] A. Kärki and S. Paulamäki. *Petrology of Olkiluoto*. Posiva OY, 2006. ISBN: 9516521436.

[17] B. Gokhale. *Rotary Drilling and Blasting in Large Surface Mines*. CRC Press, 2010. ISBN: 9780203841396.

[18] Saanio and Riekkola Consulting Engineers. "Strength and deformation properties". In: *Engineering rock mass classification of the Olkiluoto investigation site*. Ed. by K. Äikäs. Posiva, 2000. Chap. 4.1.5. ISBN: 9516520944.

[19] R. D. Knight. *Physics for Scientists and Engineers*. 2nd ed. San Francisco: Pearson Addison Wesley, 2008. ISBN: 9780321507808.

[20] B. Bhushan. *Principles and Applications to Tribology*. 2nd ed. Tribology Series. Wiley, 2013. ISBN: 9781118403006.

[21] A. Afrouz. *Practical Handbook of Rock Mass Classification Systems and Modes of Ground Failure*. Taylor & Francis, 1992. ISBN: 9780849337116.

[22] O. Ben-David and J. Fineberg. "Static Friction Coefficient Is Not a Material Constant". In: *Phys. Rev. Lett.* 106 (25 June 2011), p. 254301. DOI: 10.1103/PhysRevLett.106.254301.

[23] D. Dowson. *History of Tribology*. 2nd ed. John Wiley & Sons, 1998. ISBN: 9781860580703.

[24] T. A. Stolarski. *Tribology in Machine Design*. Referex Engineering. Butterworth Heinemann, 1990. ISBN: 9780750636230.

[25] A. M. Homola et al. "Fundamental experimental studies in tribology: The transition from "interfacial" friction of undamaged molecularly smooth surfaces to "normal" friction with wear". In: *Wear* 136.1 (1990), pp. 65–83. DOI: 10.1016/0043-1648(90)90072-I.

[26] E. E. Bisson. *Friction, Wear, and the Influence of Surfaces*. Technical Report NASA-TM-X-52380. NASA, 1967.

[27] E. Rabinowicz. *Friction and Wear of Materials*. 2nd ed. A Wiley-Interscience publication. Wiley, 1995. ISBN: 9780471830849.

[28] J. Douillard, T. Zoungrana, and S. Partyka. "Surface Gibbs free energy of minerals: some values". In: *Journal of Petroleum Science and Engineering* 14.1 (1995), pp. 51–57. DOI: 10.1016/0920-4105(95)00018-6.

[29] J. Taylor. *An Introduction to Error Analysis: The Study of Uncertainties in Physical Measurements*. 2nd ed. University Science Books, 1997. ISBN: 9780935702750.

[30] T. Riikilä et al. "Effective friction of a fracturing shear zone: Simulations and experiments". unpublished.

[31] Rules for presenting the measured value and the uncertainty. *University of Jyväskylä, Department of Physics*. Retrieved 27 November, 2016. URL: http://r.jyu.fi/2rt.

Appendix A List of Samples

Table A.1. List of ground samples and their categories. Red text denotes unsuccessful measurements. Weights-column is the total mass loaded on the weight platform (including mass of the platform). Peak is the diameter of the upper sample. Lever is the distance of the force sensor from the rotation axis. Voltage V is the voltage setting of the electric motor. Pressure is calculated using the values of M and d.

Sample	**Weights M [kg]**	**Peak d [mm]**	**Lever [mm]**	**V**	**P [MPa]**
1 (A)	173.99	17.12	85	150	7.4
2 (A)	173.99	17.76	85	150	6.9
3 (B)	173.99	29.15	85	150	2.56
4 (B)	173.99	14.30	85	150	10.6
5 (B)	173.99	13.25	85	150	12.4
6 (B)	161.55	14.11	85	150	10.1
7 (B)	173.99	19.01	85	150	6.0
8 (B)	173.99	20.17	85	150	5.3
9 (B)	173.99	22.61	85	150	4.2
10 (A)	173.99	16.73	85	150	7.8
11 (D)	173.99	9.11	85	150	26
12 (C)	173.99	12.39	85	150	14.2
13 (A)	173.99	8.50	85	150	30
14 (D)	173.99	10.41	85	150	20
15 (D)	173.99	13.93	85	150	11.2
16 (D)	173.99	12.71	85	150	13.4
17 (C)	173.99	12.90	85	150	13.1
18 (C)	173.99	14.03	85	150	11.0
19 (C)	173.99	12.02	85	150	15.0
20 (C)	173.99	14.15	85	150	10.9
21 (A)	173.99	16.49	85	150	8.0
22 (A)	173.99	15.70	85	150	8.8
23 (A)	173.99	12.33	85	150	14.3

Continued on next page

Table A.1 – Continued from previous page

Sample	**Weights *M* [kg]**	**Peak *d* [mm]**	**Lever [mm]**	***V* [V]**	***P* [MPa]**
24 (B)	173.99	10.29	85	150	20
25 (B)	173.99	10.68	85	150	19
26a (B)	149.75	41.31	85	150	1.10
26b (B)	140.83	41.31	85	150	1.03
26c (B)	125.28	41.31	85	150	0.92
26d (B)	113.06	41.31	85	150	0.83
27 (B)	173.99	45.24	85	150	1.06
28 (B)	44.04	14.77	85	150	2.5
29 (B)	200.11	31.68	85	150	2.49
30 (B)	78.58	19.76	85	150	2.51
31 (B)	120.62	24.54	85	150	2.50
32 (B)	173.99	45.10	85	150	1.07
33 (B)	173.99	45.13	85	150	1.07

Appendix B Error Calculations

Sources of Error

Peak diameter $\delta d = \pm 0.0005\,\mathrm{m}$
Peak radius $\delta R = \pm 0.000\,25\,\mathrm{m}$
Mass of weights $\delta M = \pm 0.01\,\mathrm{kg}$
NI USB-6008 (-10–10 V) accuracy 7.73 mV (as stated by the manufacturer)
Imada DS2-110 accuracy ±0.2 % F.S. (as stated by the manufacturer)
IRCON minIRT accuracy 2 °C if under 100 °C (as stated by the manufacturer)

Pressure

$$P = \frac{F}{A} = \frac{Mg}{\pi R^2} = \frac{Mg}{\pi \left(\frac{d}{2}\right)^2} \tag{B.1}$$

$$\begin{aligned} \delta P &= \sqrt{\left(\delta M \cdot \frac{\partial P}{\partial M}\right)^2 + \left(\delta d \cdot \frac{\partial P}{\partial d}\right)^2} \\ &= \sqrt{\left(\delta M \cdot \frac{g}{\pi \left(\frac{d}{2}\right)^2}\right)^2 + \left(\delta d \cdot (-2) \cdot \frac{4Mg}{\pi d^3}\right)^2} \end{aligned} \tag{B.2}$$

Torque

The length of the lever is assumed to be constant, i.e. exactly 0.085 m. Full scale of the analog output of the force sensor is -1–1 V, i.e. -500–500 N. The error caused by the sensor is

$$1\,\mathrm{V} \cdot 0.002 = 0.002\,\mathrm{V}. \tag{B.3}$$

NI USB-6008 has an accuracy of 7.73 mV. The maximum error is

$$0.002\,\mathrm{V} + 0.007\,73\,\mathrm{V} = 0.009\,73\,\mathrm{V}. \tag{B.4}$$

The voltage is converted into Newtons by multiplying it by 500. The error of the torque is

$$\delta\tau = 0.009\,73\,\mathrm{V} \cdot 500 \cdot 0.085\,\mathrm{m} = 0.413\,525\,\mathrm{Nm}. \tag{B.5}$$

Coefficient of Friction

$$\mu_k = \frac{3\tau}{Mgd}, \tag{B.6}$$

$$\begin{aligned}\delta\mu_k &= \sqrt{\left(\delta\tau \cdot \frac{\partial\mu}{\partial\tau}\right)^2 + \left(\delta M \cdot \frac{\partial\mu}{\partial M}\right)^2 + \left(\delta d \cdot \frac{\partial\mu}{\partial d}\right)^2} \\ &= \sqrt{\left(\delta\tau \cdot \frac{3}{Mgd}\right)^2 + \left(\delta M \cdot \frac{-3\tau}{M^2gd}\right)^2 + \left(\delta d \cdot \frac{-3\tau}{Mgd^2}\right)^2}\end{aligned} \tag{B.7}$$

Temperature

All measured values were under 100 °C. According to the sensor manufacturer the error is

$$\delta T = 2\,^\circ\mathrm{C}. \tag{B.8}$$

Appendix C Mean Torques and Friction Coefficients

Table C.1. Mean torques, mean friction coefficients, and pressures of samples 1–33. Error values for torque and the coefficient of friction are calculated for the mean value of each sample. Values are rounded using guidelines of University of Jyväskylä [31]. Red text denotes unsuccessful measurements.

Sample	P [MPa]	δP	τ [Nm]	$\delta\tau$	μ_k	$\delta\mu_k$
1 (A)	7.4	0.4	3.2	0.5	0.328	0.002
2 (A)	6.9	0.4	3.6	0.5	0.356	0.002
3 (B)	2.56	0.09	7.9	0.5	0.4762	0.0007
4 (B)	10.6	0.7	3.3	0.5	0.401	0.003
5 (B)	12.4	1.0	9.5	0.5	1.25749	0.006
6 (B)	10.1	0.8	2.9	0.5	0.387	0.004
7 (B)	6.0	0.4	4.7	0.5	0.430	0.002
8 (B)	5.3	0.3	5.2	0.5	0.4504	0.0014
9 (B)	4.2	0.2	5.7	0.5	0.4448	0.0012
10 (A)	7.8	0.5	5.1	0.5	0.537	0.002
11 (D)	26	3	2.2	0.5	0.426	0.007
12 (C)	14.2	1.2	3.5	0.5	0.496	0.004
13 (A)	30	4	2.1	0.5	0.444	0.008
14 (D)	20	2	2.7	0.5	0.460	0.006
15 (D)	11.2	0.9	5.6	0.5	0.711	0.004
16 (D)	13.4	1.1	5.6	0.5	0.772	0.005
17 (C)	13.1	1.1	4.4	0.5	0.597	0.004
18 (C)	11.0	0.8	4.8	0.5	0.603	0.004
19 (C)	15.0	1.3	2.4	0.5	0.345	0.004
20 (C)	10.9	0.8	4.0	0.5	0.498	0.003
21 (A)	8.0	0.5	5.2	0.5	0.555	0.003
22 (A)	8.8	0.6	3.5	0.5	0.394	0.003
23 (A)	14.3	1.2	3.2	0.5	0.450	0.004
24 (B)	20	2	5.0	0.5	0.863	0.007
25 (B)	19	2	2.1	0.5	0.340	0,005

Continued on next page

Table C.1 – Continued from previous page

Sample	P [MPa]	δP	τ [Nm]	$\delta\tau$	μ_k	$\delta\mu_k$
26a (B)	1.10	0.03	5.7	0.5	0.2799	0.0004
26b (B)	1.03	0.03	4.6	0.5	0.2422	0.0005
26c (B)	0.92	0.03	3.2	0.5	0.1918	0.0006
26d (B)	0.83	0.03	2.9	0.5	0.1913	0.0008
27 (B)	1.06	0.03	13.9	0.5	0.5406	0.0003
28 (B)	2.5	0.2	1.2	0.5	0.58	0.04
29 (B)	2.49	0.08	9.3	0.5	0.4512	0.0004
30 (B)	2.51	0.13	2.7	0.5	0.535	0.007
31 (B)	2.50	0.11	3.9	0.5	0.398	0.002
32 (B)	1.07	0.03	15.2	0.5	0.5914	0.0003
33 (B)	1.07	0.03	16.9	0.5	0.6586	0.0003

Appendix D Torque and Friction Coefficient Figures

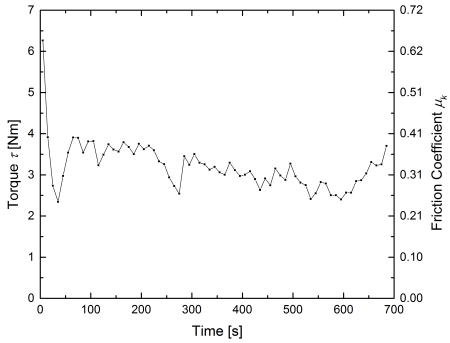

(a) Sample 1

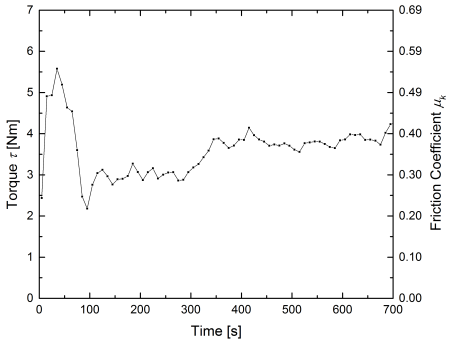

(b) Sample 2

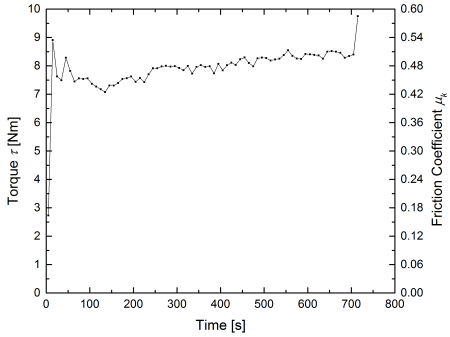

(c) Sample 3

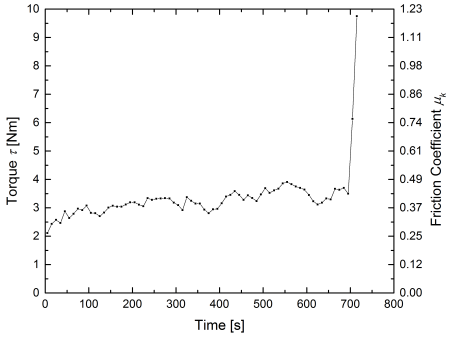

(d) Sample 4

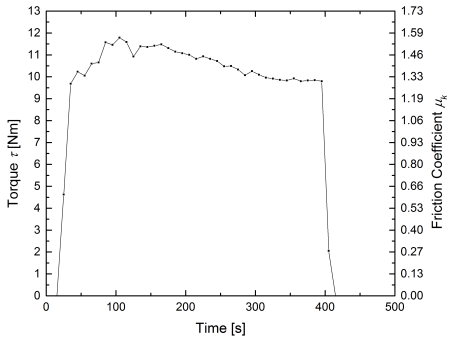

(e) Sample 5

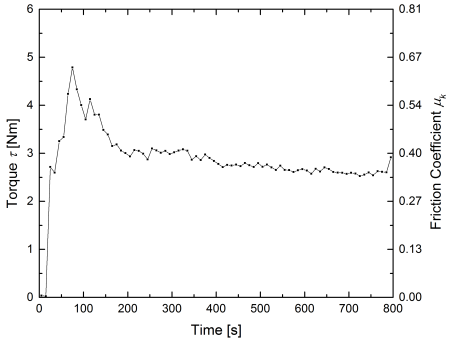

(f) Sample 6

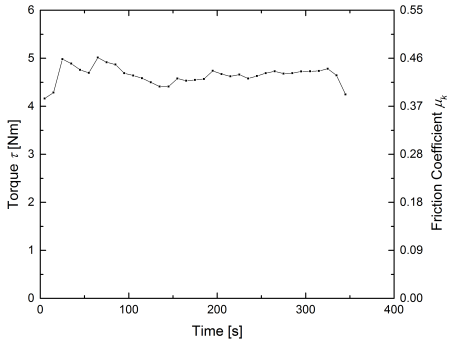

(a) Sample 7

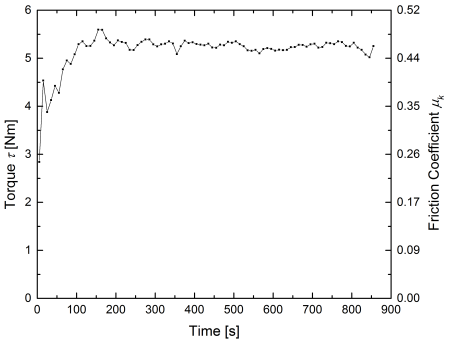

(b) Sample 8

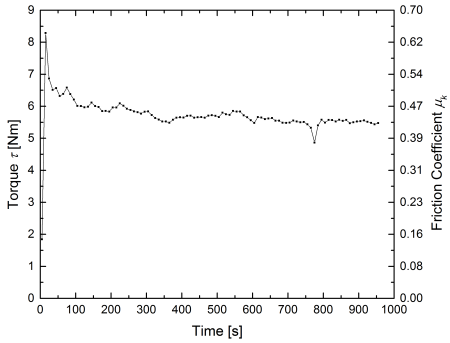

(c) Sample 9

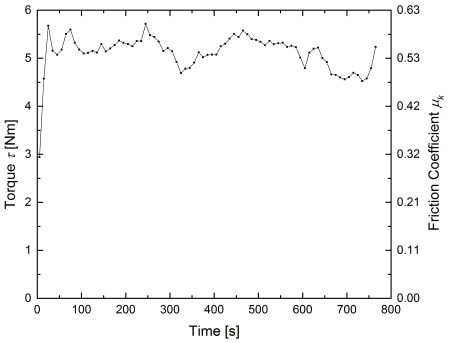

(d) Sample 10

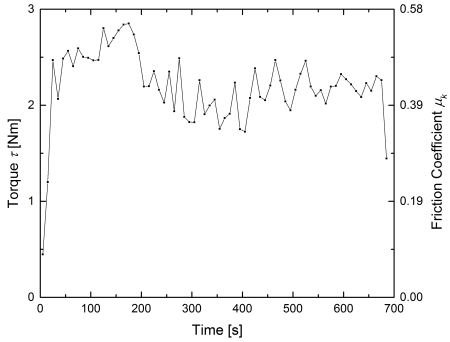

(e) Sample 11

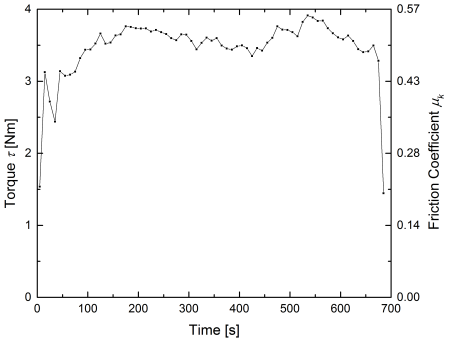

(f) Sample 12

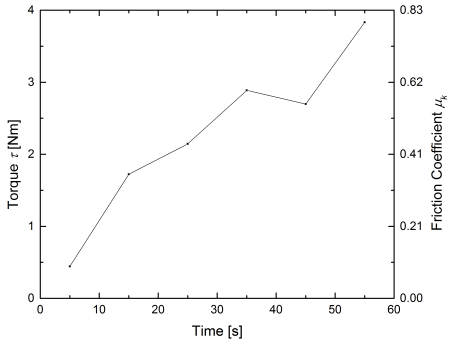

(a) Sample 13

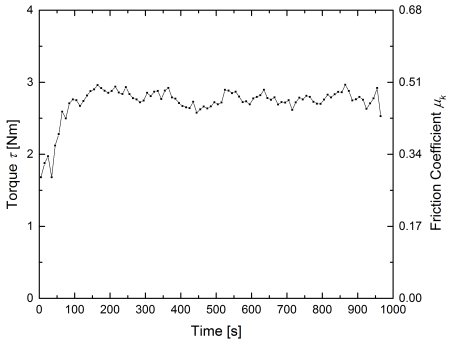

(b) Sample 14

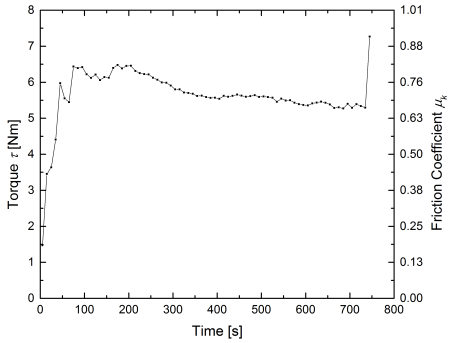

(c) Sample 15

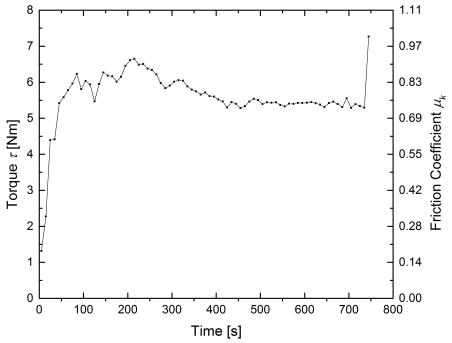

(d) Sample 16

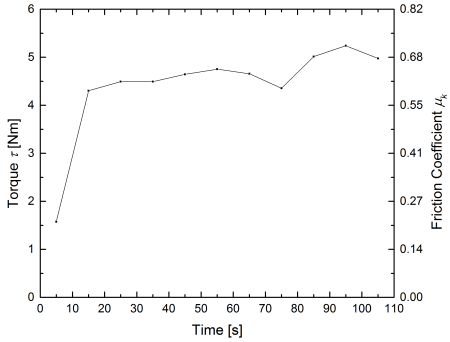

(e) Sample 17

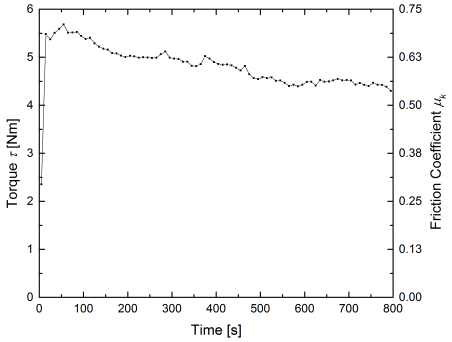

(f) Sample 18

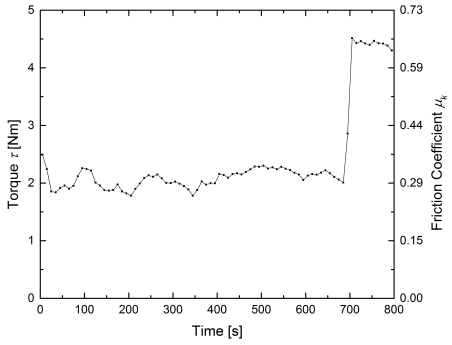

(a) Sample 19

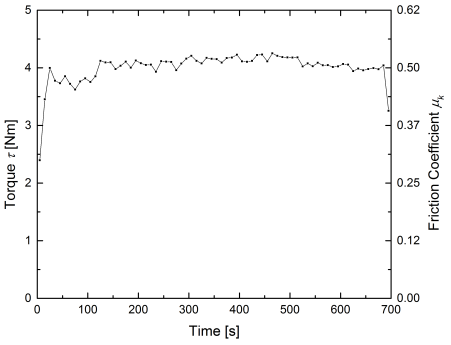

(b) Sample 20

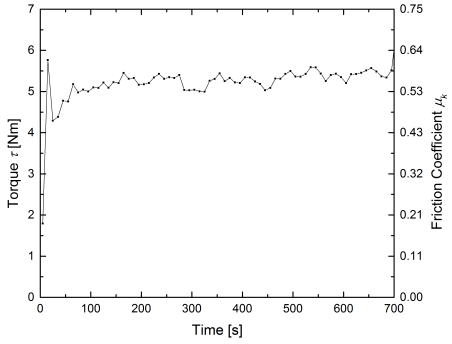

(c) Sample 21

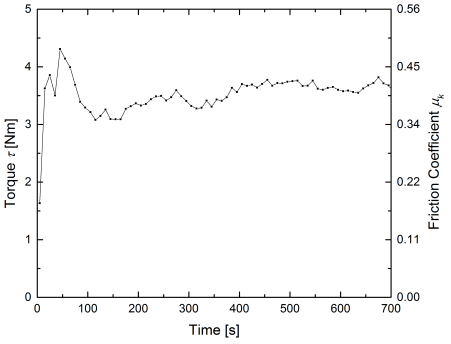

(d) Sample 22

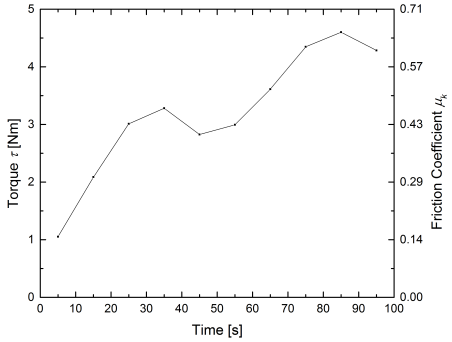

(e) Sample 23

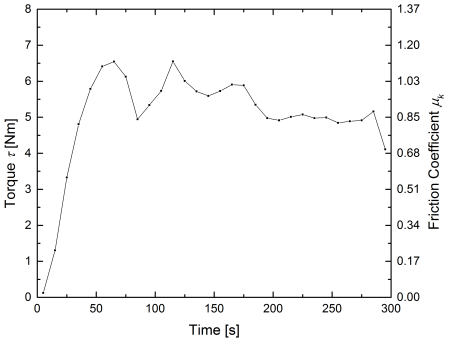

(f) Sample 24

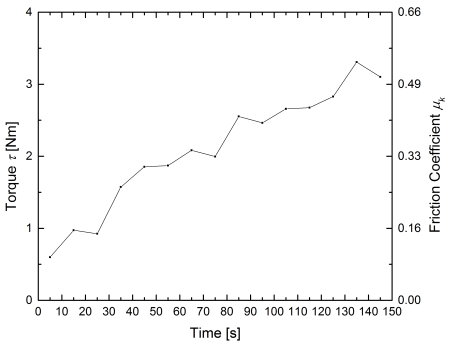

(a) Sample 25